

# Complementing XCO<sub>2</sub> imagery with ground-based CO<sub>2</sub> and <sup>14</sup>CO<sub>2</sub> measurements to monitor CO<sub>2</sub> emissions from fossil fuels on a regional to local scale

Elise Potier<sup>1</sup>, Grégoire Broquet<sup>1</sup>, Yilong Wang<sup>1,2</sup>, Diego Santaren<sup>1</sup>, Antoine Berchet<sup>1</sup>, Isabelle Pison<sup>1</sup>, Julia Marshall<sup>3</sup>, Philippe Ciais<sup>1</sup>, François-Marie Bréon<sup>1</sup>, and Frédéric Chevallier<sup>1</sup>

<sup>1</sup>Laboratoire des Sciences du Climat et de l'Environnement, LSCE/IPSL, CEA-CNRS-UVSQ, Université Paris-Saclay, F-91191 Gif-sur-Yvette, France

<sup>2</sup>Key Laboratory of Land Surface Pattern and Simulation, Institute of Geographical Sciences and Natural Resources Research, Chinese Academy of Sciences, Beijing, China.

<sup>3</sup>Max Planck Institute for Biogeochemistry (MPI-BGC), Jena, Germany. Now at Deutsches Zentrum für Luft- und Raumfahrt (DLR), Institut für Physik der Atmosphäre, Oberpfaffenhofen, Germany

**Correspondence:** Elise Potier (elise.potier@lscce.ipsl.fr)

**Abstract.** Various satellite imagers of the vertically integrated column of carbon dioxide (XCO<sub>2</sub>) are under development to enhance the capabilities for the monitoring of the fossil fuel (FF) CO<sub>2</sub> emissions. XCO<sub>2</sub> images can be used to detect plumes from cities and large industrial plants, and to quantify the corresponding emissions using atmospheric inversions techniques. However, this potential and the ability to catch the signal from more diffuse FF CO<sub>2</sub> sources can be hampered by the mix  
5 between these FF signals and a background signal from other types of CO<sub>2</sub> surface fluxes, and in particular of biogenic CO<sub>2</sub> fluxes. The deployment of dense ground-based air-sampling networks for CO<sub>2</sub> and radiocarbon (<sup>14</sup>CO<sub>2</sub>) could complement the spaceborne imagery by supporting the separation between the fossil fuel and biogenic or biofuel (BF) CO<sub>2</sub> signals. We evaluate this potential complementarity with a high resolution analytical inversion system focused on Northern France, Western Germany, Belgium, Luxembourg and a part of the Netherlands, and with pseudo-data experiments. The inversion system  
10 controls the FF and BF emissions from the large urban areas and plants, in addition to regional budgets of more diffuse emissions or of biogenic fluxes (NEE, Net Ecosystem Exchange), at an hourly scale over a whole day. The system [provides results corresponding to the assimilation ofassimilates](#) pseudo data from a single track of a 300-km swath XCO<sub>2</sub> imager at 2 km resolution and from surface ground-based CO<sub>2</sub> and/or <sup>14</sup>CO<sub>2</sub> networks. It represents the diversity of <sup>14</sup>CO<sub>2</sub> sources and sinks and not just the dilution of radiocarbon-free FF CO<sub>2</sub> emissions. The uncertainty in the resulting FF CO<sub>2</sub> emissions at  
15 local (urban area/ plant) to regional scales is directly derived and used to assess the potential of the different combinations of observation systems. The assimilation of satellite observations yield estimates of the morning regional emissions with an uncertainty down to 10% (1 sigma) in the satellite field of view, from an assumed uncertainty of 15% in the prior estimates. However, it does not provide direct information about emissions outside the satellite field of view and neither about afternoon or nighttime emissions. The co-assimilation of <sup>14</sup>CO<sub>2</sub> and CO<sub>2</sub> [surface observationsdata](#) leads to a further reduction of the  
20 uncertainty in the estimates of FF emissions. However, this further reduction is significant only in administrative regions with three or more <sup>14</sup>CO<sub>2</sub> and CO<sub>2</sub> sampling sites. The uncertainty <sup>14</sup> in the estimates of 1-day emission in North Rhine-Westphalia,

a region with three sampling sites, decreases from 8 to 6.6% when assimilating the in situ  $^{14}\text{CO}_2$  and  $\text{CO}_2$  data in addition to the satellite data. Furthermore, this [additional](#) decrease appears to be larger when the ground stations are close to large FF emission areas, providing an additional direct constraint for the estimate of these sources rather than supporting the characterization of the background signal from the NEE and its separation from that of the FF emissions. [More generally, the results indicate no amplification of the potential of each observation subsystem when they are combined into a large observation system with satellite and surface data.](#)

## 1 Introduction

Article 4 of the Paris Climate Agreement aims to reduce greenhouse gas (GHG) emissions within a few decades on the basis of equity, until they are compensated by GHG removals. The monitoring of this international ambition implies some operational observation of the GHG emissions, in particular those of carbon dioxide ( $\text{CO}_2$ ) from fossil fuels (FFs). A significant contribution to this monitoring is expected from observations of atmospheric composition and atmospheric inversion systems (IPCC, 2019; Ciais et al., 2015; Pinty et al., 2017). In particular, the development of spaceborne imagery of the vertically integrated column of  $\text{CO}_2$  ( $\text{XCO}_2$ ), at spatial resolution better than 5 km, should make it possible to detect plumes [downwind from under the wind from](#) anthropogenic sources of  $\text{CO}_2$  (Pillai et al., 2016; Schwandner et al., 2017; Broquet et al., 2018). A key example of such imagery is the Copernicus Anthropogenic Carbon Dioxide Monitoring ([CO2M](#); [Pinty et al., 2017](#); [Kuhlmann et al., 2019](#); [Lespinas et al., 2020](#)) (~~[Pinty et al., 2017](#)~~) constellation which is schedule to launch in 2025-2026. Each satellite of the constellation will observe  $\text{XCO}_2$  with a  $\sim 300$  km swath and a  $\sim 2 \times 2$  km<sup>2</sup> spatial resolution.

Previous analyses of the potential of high resolution satellite imagery of  $\text{XCO}_2$  (such as [ESA, 2015](#); [Wang et al., 2020](#); [Santaren et al., 2021](#)) (~~[Broquet et al., 2018](#)~~) (~~[Kuhlmann et al., 2019](#)~~) have focused on its use as a stand-alone observation system, and on the potential complementarity of images of co-emitted species co-registered with an instrument onboard the same satellite or from another mission ([Reuter et al., 2019](#); [Kuhlmann et al., 2019, 2020](#)). However, the distinction between FF and natural  $\text{CO}_2$  signals and thus the separation between the FF and natural components in the flux estimates remain difficult, even when using high-resolution images and satellite data on co-emitted species ([Kuhlmann et al., 2020](#); [Santaren et al., 2021](#); [Sadiq et al., 2021](#)) (~~[Santaren et al., 2021](#)~~). The separation between the emissions from biofuel (BF) and FF combustion is another challenge because BF emissions can be located in the same hot-spots as FF ones (Ciais et al., 2020).

The deployment of dense ground-based networks of near-surface air sampling for radiocarbon ( $^{14}\text{CO}_2$ ) has been also considered in complement to the spaceborne imagery (Ciais et al., 2015). Indeed FF-emitted  $\text{CO}_2$  is radiocarbon-free ([Pinty et al., 2017](#); [Levin et al., 2003, 2021](#)) (~~[Wang et al., 2018](#)~~; ~~[Wang et al., 2016](#)~~) (~~[Basu et al., 2016](#)~~):  $^{14}\text{CO}_2$  surface data have a less ambiguous sensitivity to the signal from FF emissions than  $\text{CO}_2$  surface data. However, practical constraints lead to sampling  $^{14}\text{CO}_2$  daily if not weekly to monthly ([Levin et al., 2020](#)). This prevents the direct identification of temporal variations at higher frequencies, e.g. hourly, associated with the signal from cities and point sources, but time series of continuous hourly measurements of  $\text{CO}_2$  should enable these specific temporal variations to be captured. [Various studies have been conducted to estimate the potential of  \$^{14}\text{CO}\_2\$  surface data in addition to  \$\text{CO}\_2\$  surface data to discriminate anthropogenic from biogenic](#)

55 CO<sub>2</sub>. Most of the studies with real samplings corresponded to local analyses (e.g. Levin et al., 2003; Turnbull et al., 2006; Lehman et al., 2013; Wenger et al., 2019; Lee et al., 2020). Inversions with pseudo data were used to assess the potential of <sup>14</sup>CO<sub>2</sub> surface data to monitor the FF CO<sub>2</sub> emissions at continental scales (Wang, 2016; Wang et al., 2018; Basu et al., 2016). However, Graven et al. (2018) or Basu et al. (2020) showed promising results regarding the quantification of budgets of FF CO<sub>2</sub> emissions or the assessment of their estimates from inventories based on ~10 stations of <sup>14</sup>CO<sub>2</sub> at the scale of California or of the United States, respectively.

60 This study aims at assessing the potential of combination between a spaceborne XCO<sub>2</sub> imager and ground based <sup>14</sup>CO<sub>2</sub> and CO<sub>2</sub> networks to monitor FF emissions of CO<sub>2</sub> at finer spatial scales, typically that of administrative regions in Europe, and with a view to feed operational systems with highly accurate emission estimates. More specifically, it aims at assessing how these additional ground-based networks decrease the uncertainty in FF emissions by improving the distinction between the FF and biogenic fluxes.

65 There is currently no XCO<sub>2</sub> large swath imager in orbit and we assume that dense networks of <sup>14</sup>CO<sub>2</sub>, with more stations than the current ones even in areas relatively well equipped like Europe ((Levin et al., 2020), <https://www.icos-cp.eu/>), are required to support such monitoring of the FF CO<sub>2</sub> emissions. Furthermore, the combination of remote sensing data and air sample measurements has often been difficult, mainly due to systematic errors in satellite retrievals and in the atmospheric chemistry-transport models that simulate them. In this case, the air sample measurements are rather used to constrain some bias correction of the remote sensing data (Bergamaschi et al., 2009) and/or the model (Locatelli et al., 2015); or they are implicitly used to dampen the effect of these systematic errors. The gradual improvement in the quality of retrievals and models over time has just recently opened the door to a more harmonious use of remote sensing data and air sample measurements for inverse modelling (Byrne et al., 2022).

70 Therefore, this study relies on inversion tests performed with parameters corresponding to pseudo-observations and different scenarios of observation systems, i.e., on Observing System Simulation Experiments (OSSEs). The analysis focuses on the strengths and limitations of the atmospheric sampling from the different measurement systems. It discards components of the uncertainties associated to the current atmospheric radiative transfer inversion systems, used to retrieve XCO<sub>2</sub> data from satellite measurements, and to the current atmospheric transport models underlying the atmospheric inversion. ~~The inversion tests performed in this study with different sets of pseudo-data correspond to Observing System Simulation Experiments (OSSEs). Our OSSEs~~They include the simulation of the sampling of a CO<sub>2</sub>M-like spaceborne instrument from single orbits over Western Europe at 12:00 (Universal Time Coordinated, UTC) and a scenario of dense CO<sub>2</sub> and <sup>14</sup>CO<sub>2</sub> ground-based network.

75 The work performed relies on a Bayesian inversion framework, in which the knowledge of control parameters, here the CO<sub>2</sub> fluxes, improves with the assimilation of related observations. It is focused on the direct computation of the uncertainty in the control parameters. We analyse the uncertainty in the *posterior* values of the control parameters as a function of the observation system that is used for the inversion, and the corresponding uncertainty reduction, i.e., the relative difference between the posterior uncertainty and the prior uncertainty in the control parameters. The analysis of this uncertainty reduction is made over one day at the local scale (urban areas, industrial plants) to the scale of administrative regions in Europe regional

90 ~~scale~~, following the rationale and the general inverse modelling framework of Santaren et al. (2021). It focuses on a large part of Western Europe, using a ~~regional atmospheric transport model-configuration-of-the-CHIMERE-regional-transport-model (Menut et al., 2013)~~ with a 2 km horizontal zoom over Northern France, Western Germany, Belgium, Luxembourg and a large part of the Netherlands. ~~It controls FF emissions from urban areas and industrial plants in addition to regional budgets of more diffuse emissions or of biogenic fluxes at an hourly scale. The analytical expression of the inversion framework~~  
95 ~~(Wu et al., 2016) allows for the results of the individual control parameters or for budgets integrated in space within the regions or in time within a day to be analyzed and for many options for the observation system to be tested despite the dimension of the high resolution inversion problem.~~

The assimilation of  $^{14}\text{CO}_2$  and  $\text{CO}_2$  surface data in addition to  $\text{XCO}_2$  images and the inclusion of non-FF fluxes of  $^{14}\text{CO}_2$  in the inversion framework make use of the larger-scale inversion framework developed by Wang (2016). It takes into account  
100 not only the  $^{14}\text{CO}_2$  emissions from nuclear power plants and fuel reprocessing plants, but also the specific isotopic signatures of the heterotrophic respiration (HR) and Net Primary Production (NPP) by land ecosystems (Miller et al., 2012; Basu et al., 2016, 2020) and thus solves for these fluxes separately. It also controls the emissions from BF burning.

The analytical inversion framework is described in section 2. Results from the pseudo-data experiments with the assimilation of satellite observations alone are taken as a reference and presented in Section 3.1. Then a larger suite of experiments  
105 combining  $^{14}\text{CO}_2$  and  $\text{CO}_2$  surface and  $\text{XCO}_2$  satellite observations is used to assess their complementarity in Sections 3.2 to 3.3. Section 4 provides some discussions about this inversion framework and a conclusion regarding complementarity of  $\text{XCO}_2$  satellite,  $^{14}\text{CO}_2$  and  $\text{CO}_2$  surface observations.

## 2 Methodology of the inversion

This section presents the high dimensional inversion framework designed in this study for the co-assimilation of  $\text{CO}_2$  and  
110  $^{14}\text{CO}_2$  data. It has strong similarities with the system developed by Santaren et al. (2021), which assimilates  $\text{CO}_2$  data only, and it borrows from Wang (2016) to assimilate  $^{14}\text{CO}_2$  data. The system relies on:

- ~~A local to regional scale~~An analytical inversion framework (Wu et al., 2016) as presented in Section 2.1, ~~which controls anthropogenic emissions from large cities and industrial plants in addition to regional budgets of more diffuse emissions or of natural fluxes in which budgets of surface anthropogenic and natural fluxes are controlled at local (city or industrial plant) or regional scales and~~ at hourly resolution (see the definition of the control vector in Section 2.5).  
115
- A zoomed configuration of the regional atmospheric transport model CHIMERE (Menut et al., 2013) for most of Western Europe, described in section 2.2.
- Hourly to annual maps of all types of surface  $\text{CO}_2$  and  $^{14}\text{CO}_2$  fluxes, at high spatial resolution from the  $\text{CO}_2$ Human Emissions project (CHE, <https://www.che-project.eu/>), which are described in section 2.3, ~~at temporal resolutions up to~~  
120 ~~1-hour~~. They are used to distribute the local-to-regional-scale budgets of the fluxes into corresponding high resolution flux maps (see section 2.5).

– Simulations of the locations [time](#) and uncertainty of the XCO<sub>2</sub> retrievals and of the CO<sub>2</sub> and <sup>14</sup>CO<sub>2</sub> ground-based data [as a function of time](#), for different scenarios of the observing system, as described in Section 2.6. For the XCO<sub>2</sub> data, we rely on the simulation of the CO2M sampling during one satellite pass over the area of interest generated by the Institut für Umweltphysik [Bremen](#) (IUPB) in the frame of the ESA-PMIF project (European Spacial Agency, Plume Monitoring Inversion Framework Wang et al., 2020; Lespinas et al., 2020).

Inversions are conducted over a 1-day window from 0:00 to 24:00, on July 1 2015, i.e. in summer when the biogenic fluxes are relatively high. The restriction to 1 day is connected to results of Santaren et al. (2021), which show the lack of sensitivity of observations made during a given day to the fluxes during other days over the modeling domain, and to the large computation cost associated with the preparation of a full day of analytical inversion. With such an inversion window, wider than the one chosen in Broquet et al. (2018) or Santaren et al. (2021), the system tracks the signal from the FF emissions up to 12 hours before the satellite overpass (see Section 2.6.1) and 10 hours before the in-situ data assimilation window (see Section 2.6.2). After a few hours, the air masses having been transported over [typically ~30-100 km](#)~~typically 100km~~, the signal from individual FF CO<sub>2</sub> sources (industrial plants, cities, regions) is much diffused and hardly detectable in XCO<sub>2</sub> images. Consequently this 1-day timescale is large enough to represent the full extent of the CO<sub>2</sub> FF plumes that can be exploited in images from CO2M-like instruments to compute the corresponding emissions (Broquet et al., 2018; Santaren et al., 2021). The ability to track large-scale budgets of FF emissions over longer time periods relies on complementary observations of FF emission tracers. These tracers, such as the <sup>14</sup>CO<sub>2</sub> measurements considered here, may help filter a relatively low FF signal from the biogenic signal, which is generally much larger over long distances (Pinty et al., 2017; Palmer et al., 2006; Fortems-Cheiney et al., 2021; Sadiq et al., 2021)~~(Pinty et al., 2017)(Fortems-Cheiney et al., 2021)~~. CO<sub>2</sub> and <sup>14</sup>CO<sub>2</sub> ground-based networks could also reinforce the constraint on the FF CO<sub>2</sub> emission estimates during the few hours before the satellite overpass. By starting the inversion window 12 hours before the satellite overpass and 10 hours before the first surface measurement, we account for the full window of FF CO<sub>2</sub> emission, the estimate of which can potentially be directly constrained by these different datasets or by their combination.

## 145 **2.1 Inversion general equation**

Under the assumption that all uncertainties in the inversion problem have a Gaussian and unbiased distribution, these uncertainties are fully characterized by their covariance matrices. [The inversion uses an observation operator to connect the control parameters \(the flux budgets, see section 2.5\) to the observation vector \(the space defined by the ensemble of pseudo observations, see section 2.6\). Here, by construction, the observation operator is linear and is denoted  \$\mathbf{H}\$ . On this basis, the analytical Bayesian inversion allows for the computation of the covariance matrix of the posterior uncertainty \(uncertainty in the posterior estimate of the fluxes\)  \$\mathbf{A}\$  as a function of  \$\mathbf{H}\$](#) ~~The analytical Bayesian inversion allows for the computation of the covariance matrix of the posterior uncertainty (uncertainty in the posterior estimate of the fluxes)  $\mathbf{A}$  as a function of the observation operator  $\mathbf{H}$  connecting the control parameters (the flux budgets, see section 2.5) to the observation vector (the space defined by the ensemble of pseudo observations, see section 2.6), of the covariance matrix of the prior uncertainty~~uncertainties (uncer-

155 tainty in the prior estimate of the fluxes, see section 2.5.2)  $\mathbf{B}$  and of the model and observation errors covariance matrix  $\mathbf{R}$  (in the observation space, see section 2.6.3), following Tarantola (2005):

$$\mathbf{A} = [\mathbf{B}^{-1} + \mathbf{H}^T \mathbf{R}^{-1} \mathbf{H}]^{-1} \quad (1)$$

The observation operator  $\mathbf{H}$ , ~~is assumed to be linear and~~ is decomposed, following the notations of Stauffer et al. (2016), into :

$$\mathbf{H} = \mathbf{H}_{sample} \mathbf{H}_{transp} \mathbf{H}_{distr} \quad (2)$$

160  $\mathbf{H}_{distr}$  defines (i) the spatial and temporal distribution of the fluxes within each area corresponding to a control parameter and beyond the temporal resolution of these control parameters, (ii) the flux budgets to be rescaled by the inversion for these areas at the control resolution, and (iii) the application of the isotopic signatures to  $\text{CO}_2$  fluxes. Here, ~~this operator~~ is based on the flux products and on the signatures described in Section 2.3.

165  $\mathbf{H}_{transp}$  is the atmospheric transport operator, corresponding to our configuration of the transport model CHIMERE described in section 2.2.

$\mathbf{H}_{sample}$  corresponds to the computation of  $\text{XCO}_2$  and to the sampling of  $\text{XCO}_2$  or of near ground ~~mole fraction~~ concentrations of  $\text{CO}_2$  and  $^{14}\text{CO}_2$  at the observation time and locations from the output of the CHIMERE model. Section 2.6 provides more details on this operator.

~~The derivation of the  $\mathbf{H}$  matrix in the analytical system requires an extensive set of simulations with the computation of the imprint (columns of  $\mathbf{H}$ ) of each of the control parameters (Santaren et al., 2021). The  $\mathbf{H}$  observation operator matrix is built explicitly to solve for Eq. (1) analytically, which requires an extensive set of simulations. The different columns of  $\mathbf{H}$  correspond to the imprints in the observation space of the different control variables. They are computed by applying the sequence of operators  $\mathbf{H}_{distr}$ ,  $\mathbf{H}_{transp}$  and then  $\mathbf{H}_{sample}$  to each control variable set to 1, keeping the others null (Broquet et al., 2018). In practice, the application of the  $\mathbf{H}_{transp}$  operator corresponds to passive tracer transport simulations with the~~  
175 ~~CHIMERE model which bears non-linearities that are assumed to be negligible (see section 2.2.1), and thus which is assumed to be well emulated via the building of  $\mathbf{H}$ . A generalized  $\mathbf{H}$  matrix is actually stored for the analytical inversion system to anticipate any option for  $\mathbf{H}_{sample}$  or for the control vector, by recording the full fields from the application of  $\mathbf{H}_{distr} \mathbf{H}_{transp}$  to all control variables considered in this study.~~

180 By focusing on the analysis of uncertainties in the control parameters, this study requires the application of Eq. (1) but not the actual computation of emission estimates based on synthetic data. The computation of  $\mathbf{H}$  is the main and most demanding step in the preparation of the inversion system. In addition to this computation, the application of Eq. (1) only requires the derivation of the  $\mathbf{B}$  and  $\mathbf{R}$  matrices, and the inversions of positive-definite matrices corresponding to the control space. This analytical expression of the inversion framework allows for the uncertainties in the individual control parameters or for budgets of emissions integrated in space or in time to be analyzed and for many options for the observation system to be tested despite  
185 the dimension of the high resolution inversion problem.

## 2.2 Atmospheric transport

### 2.2.1 Transport model configuration

The transport operator of  $\text{CO}_2$  and  $^{14}\text{CO}_2$  in the atmosphere,  $\mathbf{H}_{transport}$ , relies on the CHIMERE transport model, driven here by the Community Inversion Framework (CIF, Berchet et al., 2021). The domain and the horizontal grid for the CHIMERE configuration used here are represented in Fig. Figure 1. The domain covers a part of Western Europe (longitude:  $-6.82^\circ$  to  $19.18^\circ$ ; latitude:  $42.0^\circ$  to  $56.39^\circ$ ). The resolution of the horizontal grid varies between 50 and 2 km. The  $2\text{ km} \times 2\text{ km}$ -resolution zoom covers Northern France, Luxemburg, Belgium, a large part of the Netherlands and Western Germany (longitude:  $-1.25^\circ$  to  $10.64^\circ$ ; latitude:  $47.45^\circ$  to  $53.15^\circ$ ). The vertical grid is composed of 29 pressure layers extending from the surface 997 hPa to 300 hPa (from the surface to approximately 9 km above the ground level).

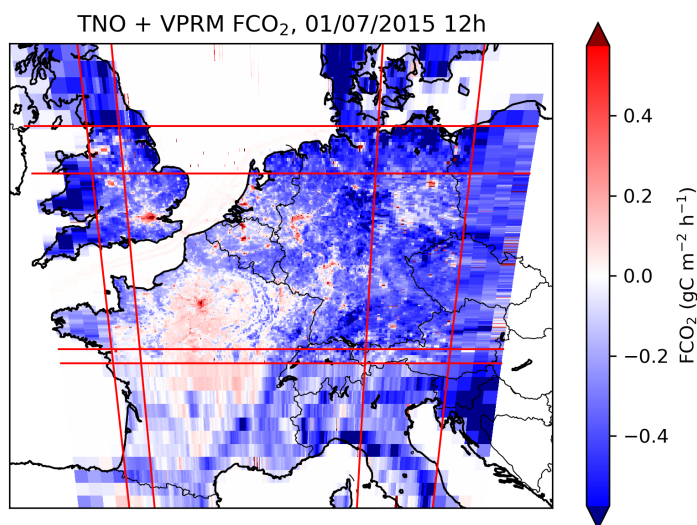


**Figure 1.**  $\text{CO}_2$  flux map (based on values from the TNO inventory and VPRM simulations for 1 July 2015 at 12:00) over the atmospheric transport modelling grid. The red lines delimit the spatial resolution changes within the domain (from 2 km to 10 km and then 50 km from the middle to the edges of the domain)

Our configuration of CHIMERE ignores chemistry since  $\text{CO}_2$  and  $^{14}\text{CO}_2$  are inert species at the time scale considered in this study (24 h). The actual transport of passive tracers is linear but non-linearities arise in the models due to their inherent discretization of the transport. However these non-linearities are small and this explains why the resulting atmospheric transport operator  $\mathbf{H}_{transport}$  is assumed to be well emulated via the building of the  $\mathbf{H}$  matrix. CHIMERE is forced by meteorological variables provided by the European Centre for Medium-Range Weather Forecasts (ECMWF) for the CHE project at 9 km

200 resolution (Agusti-Panareda, 2018). Figure 2 provides indications on the typical horizontal transport conditions during the day of inversions over the area of interest: on July 1<sup>st</sup> 2015, a South-East wind over the North East part of the domain spreads the atmospheric signature of FF emissions in the North-West direction.

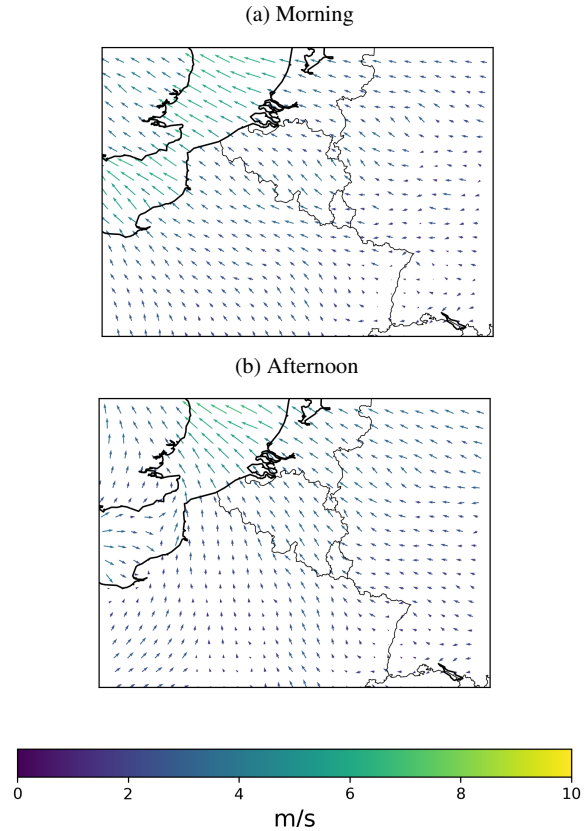


**Figure 2.** Morning (a) and afternoon (b) wind averaged in the first two vertical layers of the CHIMERE grid (i.e., heights between 0 and 28 m above the ground)

### 2.2.2 Simulation of CO<sub>2</sub> and <sup>14</sup>CO<sub>2</sub> transport

In this section, we present a formal decomposition of the CO<sub>2</sub> and <sup>14</sup>CO<sub>2</sub> transport in order to introduce the notation and assumptions used in the inversion framework. The decomposition of the <sup>14</sup>CO<sub>2</sub> transport and its formulation in a specific unit (parts per million per mil, ppm ‰) follow that of Wang (2016).

$$C_a = \mathbf{H}_{transp} [F_{FF} + F_{BF} + F_{NPP} + F_{HR}] + \mathbf{H}_{bc} [C_{bc}] \quad (3)$$



$$\begin{aligned}
C_a \cdot \delta_a = & \mathbf{H}_{transp} [\delta_{FF} \cdot F_{FF} + \delta_{BF} \cdot F_{BF} + \\
& \delta_{NPP} \cdot F_{NPP} + \delta_{HR} \cdot F_{HR} + \\
& 1/R_{std} \cdot F_{Nucl}] + \\
& \mathbf{H}_{bc} [C_{bc} \cdot \delta_{bc}]
\end{aligned} \tag{4}$$

210 where:

- $C_a$  is the CO<sub>2</sub> atmospheric mole fraction concentration.
- $F_x$  terms correspond to different types  $x$  of CO<sub>2</sub> fluxes within the transport modelling domain: FF emissions, BF emissions, NPP and HR. Of note is that the sign of fluxes in this equation corresponds to the atmosphere point of view: they are positive when CO<sub>2</sub> is emitted to the atmosphere, and negative when it is absorbed from the atmosphere. In particular,  $F_{NPP}$  is positive when the NPP is negative.
- $C_{bc,x}$  are the boundary (top and lateral) and initial conditions of CO<sub>2</sub> and <sup>14</sup>CO<sub>2</sub> mole fraction concentration, and  $\mathbf{H}_{bc}$  their transport within the modeling domain, but they are ignored in this inversion study (see Section 2.3.3).
- $\delta_a$  are the <sup>14</sup>CO<sub>2</sub>/<sup>12</sup>CO<sub>2</sub> ratios in the atmosphere ( $R$ ), normalized by the <sup>14</sup>C/<sup>12</sup>C ratio in the Modern Standard (( $R/R_{std} - 1$ );  $R_{std} = 1.176 \times 10^{-12}$ ). Similarly, in the following, all  $\delta$  are also normalized ratios.
- $\delta_x$  are the <sup>14</sup>CO<sub>2</sub> isotopic signatures of the <sup>14</sup>CO<sub>2</sub> fluxes listed above.
- $F_{Nucl}$  corresponds to <sup>14</sup>CO<sub>2</sub> fluxes from nuclear power plants.

## 2.3 Flux maps

### 2.3.1 CO<sub>2</sub> flux maps

The anthropogenic CO<sub>2</sub> emissions, from both FF and BF combustion, are derived from two inventories of the annual emissions produced by Netherlands Organisation for Applied Scientific Research (TNO) over Europe for the year 2015 (Denier van der Gon et al., 2017; Super et al., 2020). These inventories provide emission maps for 15 activity sectors following the Gridded Nomenclature For Reporting (GNFR) of the United Nations Framework Convention on Climate Change (UNFCCC). The emissions in the 2-km-resolution area of the domain are interpolated from a ~1 km (1/60° × 1/120°) resolution inventory (TNO\_GHGco\_1x1km\_v1\_1) which entirely covers this area but not the whole CHIMERE domain (its extent being -2° to 19° in longitude and 47° to 56° in latitude). The emissions in the rest of the CHIMERE domain are interpolated from a ~6 km (1/10° × 1/20°) resolution inventory (TNO\_GHGco\_v1\_1, covering -30° to 60°, in longitude and 30° to 72° in latitude). These data are projected on the CHIMERE horizontal grid ensuring mass-conservation. The temporal disaggregation at hourly scale

is based on coefficients ~~provided with the TNO inventories for each depending on the~~ sector of activity and as a function of the time zones provided in the CHE project (Marshall et al., 2019). Emissions from point sources are projected on the CHIMERE vertical grid ~~with coefficients~~ depending on ~~the~~ activity sectors (Bieser et al., 2011), also provided with the TNO inventories, while emissions from diffused sectors of activity (traffic, heating etc.) are emitted from the ground in the model.

No distinctions between CO<sub>2</sub> BF emissions from woods and crops is done in the TNO inventories. However this split is needed to derive <sup>14</sup>CO<sub>2</sub> fluxes (see below). Consequently, assumptions are made based on emission categories used in TNO inventory ~~, i.e. the Gridded Nomenclature For Reporting (GNFR) of the United Nations Framework Convention on Climate Change (UNFCCC)~~. In this study, we consider that BF from woods is burned in power plants and in the industry and residential sectors only, i.e. in categories A to C. BF from crops is burned in categories F and L only, that correspond to road transport and agriculture. We assume that the BF emissions from the other sectors are negligible since they represent less than 2 % of the total BF emissions in the vast majority of countries.

The CO<sub>2</sub> biogenic fluxes are interpolated from simulations at 1 h and 5 km resolution with the VPRM model (Vegetation Photosynthesis and Respiration Model, Mahadevan et al., 2008) for the year 2015, provided by MPI-Jena over Europe (over latitude 31° to 68.7°; longitude -35.5° to 60.5°). The VPRM simulations provide estimates of gross primary production (GPP) and total respiration. ~~However, we need to split the biogenic fluxes into NPP and HR since they bear different isotopic signatures. Therefore, we recombine GPP and Respiration from VPRM into NPP and HR fluxes, using d~~ Daily partition coefficients ( $\alpha_{HR}$ ) that are derived from ORCHIDEE-MICT simulations at 0.5° resolution over Europe in 2015 (Guimberteau et al., 2018) ~~to scale GPP and Respiration from VPRM into NPP and HR fluxes~~. The total biogenic fluxes correspond to the Net Ecosystem Exchange ( $F_{NEE} = F_{NPP} + F_{HR} = F_{GPP} + F_{Resp}$ ) ( $NEE = NPP + HR = GPP + Resp$ ).

The total CO<sub>2</sub> fluxes for 1<sup>st</sup> July 2015 at 12:00 are presented in ~~Fig.~~ Figure 1.

### 2.3.2 Isotopic signatures and <sup>14</sup>CO<sub>2</sub> flux maps

To produce <sup>14</sup>CO<sub>2</sub> fluxes, corresponding isotopic signatures are applied to the CO<sub>2</sub> fluxes.

$\delta_{FF} = -1000\text{‰}$  was applied to  $F_{FF}$  on the whole year and domain.

We distinguish  $\delta_{BF,wood}$  from  $\delta_{BF,crop}$  because crops and wood have a different age at harvest resulting in different <sup>14</sup>C abundance. In a first approximation, we determined these  $\delta_{BF}$  as a spatial and temporal average of <sup>14</sup>CO<sub>2</sub> ~~contente~~ contains in vegetation,  $\delta_{biomass}$ , simulated with the emulator of the ORCHIDEE-MICT model (Guimberteau et al., 2018; Naipal et al., 2018; Wang, 2016) over the whole ORCHIDEE-MICT Europe domain in 2015, selecting the relevant plant functional types (PFT): non-tropical trees for  $\delta_{BF,wood}$  ~~and~~ crops for  $\delta_{BF,crop}$ . Such a computation of  $\delta_{BF}$  relies on the hypothesis that the wood or cropfuel burnt in Europe comes from European (López et al., 2017) and recently cut vegetation. As a result,  $\delta_{BF,wood} = 95\text{‰}$  and  $\delta_{BF,crop} = 19\text{‰}$ .

$\delta_{NPP}$  monthly maps at 5 km spatial resolution were derived for application to the VPRM biogenic fluxes:

$$\delta_{NPP} = \delta_{a,surf} - \epsilon \quad (5)$$

where  $\delta_{a,surf}$  is the radiocarbon signature in the surface atmospheric layer and  $\epsilon$  is the sum of kinetic and enzymatic  $^{14}\text{CO}_2$  fractionation with respect to  $^{12}\text{CO}_2$  depending on the C3 or C4 photosynthesis pathway of the vegetation.

270 Monthly background measurements of the radiocarbon ratio in the conventional definition ( $\Delta 14\text{C}$ , Stuiver and Polach, 1977) are available, in 2015, at Schauinsland in Germany (Hammer and Levin, 2017). The conversion to the normalized ratio,  $\delta_{a,surf}$ , is done following Stuiver and Polach (1977), with  $\delta_{13\text{C}}$  from Graven et al. (2017).  ~~$\delta_{a,surf}$  is characterized by a conversion of  $\Delta 14\text{C}$  monthly background measurements, at Schauinsland in Germany, in 2015 (Hammer and Levin, 2017) following Stuiver and Polach (1977) with  $\delta_{13\text{C}}$  from Graven et al. (2017).~~ This ratio varies between 46  
275 and 49 ‰. Here, we neglect the impact of variations of this  $\delta_{a,surf}$  at high spatial and temporal resolution on the  $^{14}\text{CO}_2$  NPP fluxes themselves. Accounting for such variations for a precise computation of the  $\delta_{NPP}$ , and so  $^{14}\text{CO}_2$  NPP fluxes, would have required a dynamical computation with  $\delta_{a,surf}$  depending on  $^{14}\text{CO}_2$  mole fraction ~~concentrations~~ calculated by the transport model and would have introduced ~~strong~~ non-linearities. Accounting for such non-linearities in the observation operator would have required a complex inversion framework including the use of synthetic data and the iterative linearization  
280 of the observation operator into an evolving **H** matrix (Wang, 2016). ~~in the inversion (with an evolving **H**).~~ However, over one day, these variabilities within each region-month are assumed to be negligible as was found by Wang (2016) ~~within each region-month~~.

The value of  $\epsilon$  is 36 ‰ for C3 vegetation and 8 ‰ for C4 vegetation as described by Wang (2016) from Farquhar et al. (1989) and Degens (1969). We derive the C3/C4 distribution on the VPRM grid and per month, from the combination of three land  
285 cover maps: the VPRM and ORCHIDEE land cover maps and monthly MIRCA2000 crop map (Portmann et al., 2010). This combination allows us to capitalise on the high spatial resolution of the VPRM land cover map at 5 km derived from SYNMAP at 1-km-resolution (Jung et al., 2006) and a more precise PFT information in ORCHIDEE land cover maps at  $0.5^\circ$  resolution to determine the C3 or C4 photosynthesis type. In case of the crop PFT, the MIRCA2000 crop map at  $\sim 0.08^\circ$ -resolution indicates the surface area covered by each crop type, and thus the relevant photosynthesis type, with a finer resolution than in  
290 ORCHIDEE and with the monthly variability of the year 2000. The resulting  $\delta_{NPP}$  varies between 10 and 41‰.

$\delta_{HR}$  daily maps for the year 2015 are derived from simulations with the above-mentioned ORCHIDEE-MICT emulator. For each grid cell, the daily  $\text{CO}_2$  and the corresponding  $^{14}\text{CO}_2$  emissions from litter respiration and 3 types of soil respiration were aggregated. Their ratio,  $\delta_{HR}$ , is then interpolated from the ORCHIDEE-MICT grid to the VPRM grid. The resulting  $\delta_{HR}$   
295 varies between 22 and 177 ‰.

Nuclear  $^{14}\text{CO}_2$  emissions are **simply** calculated following Graven and Gruber (2011) based on the annual activity of each reactor, in 2015, reported in Zazzeri et al. (2018). For each reactor, activity data  $A$  in  $\text{TBq} \cdot \text{yr}^{-1}$  is converted into  $^{14}\text{C}$  production in  $\text{kg}^{14}\text{C} \cdot \text{yr}^{-1}$   ~~$\text{kg}^{14}\text{C} \cdot \text{reactor}^{-1} \cdot \text{yr}^{-1}$~~ :

$$300 \quad F_{\text{Nucl}} = A \times \alpha \times 10^9 \quad (6)$$

with  $\alpha = R_{\text{std}}/0.226$ , where  $0.226 \text{ Bq} \cdot \text{gC}^{-1}$  is the conversion factor from activity to carbon production.

### 2.3.3 Ignoring ocean fluxes, cosmogenic production, biomass burning emissions and the regional boundary conditions

This study is focused on the analysis of uncertainties and of their propagation between the control and observation space.  
305 Therefore, the components that have to be taken into account in the transport simulation are those which bear uncertainties whose impact is accounted for or those which interfere with the transport of the components which bear uncertainties.

The impact of ~~the uncertainties~~**uncertainty** in the initial condition (at 0:00 on July 1 2015) and ~~inat~~ the boundary conditions (at the lateral and top boundaries of the CHIMERE domain) are assumed to be negligible. ~~following the results from Santaren et al. (2021)~~: The analysis by Santaren et al. (2021) suggests that the large-scale uncertainties should not have large  
310 impact on the results, due to the good distinction between smooth background signal from the initial and boundary conditions and the imprints of the local and regional fluxes. Furthermore, the fine-scale uncertainties should have a limited impact at the observation times due to the 10-hour time lag between the initial conditions and the first observations (see Section 2.6.2) and since the model boundaries are quite far from the area of interest. ~~These~~ conditions are thus ignored in the definition of our inversion problem and in the atmospheric transport operator.

315 Regarding the  $\text{CO}_2$  (and thus  $^{14}\text{CO}_2$ ) ocean fluxes, we also assume that they can be neglected here because the CHIMERE domain is mostly continental.

The cosmogenic production of  $^{14}\text{C}$  becomes significant above  $\sim 700$  hPa, well above the planetary boundary layer (Turnbull et al., 2009), while we are interested in simulating  $^{14}\text{CO}_2$  ~~mole fraction~~**concentrations** near the ground. Even though we use some high-altitude stations, we can assume that most of the influence from the cosmogenic production at these surface stations  
320 comes from the model lateral boundaries and that the cosmogenic production within the modelling domain can be neglected.

$\text{CO}_2$  and  $^{14}\text{CO}_2$  biomass burning emissions are also neglected since they are generally relatively weak in our modelling domain (especially in the 2-km resolution part of the modelling grid on which the analysis focuses).

## 2.4 Resulting $\text{CO}_2$ and $^{14}\text{CO}_2$ fields

Figure 3 illustrates the resulting signals simulated with CHIMERE at 12:00, on July 1 2015, after 12h of simulation. The  $\text{CO}_2$   
325 (Fig. 3a) and  $^{14}\text{CO}_2$  (Fig. 3b) mole fractions surface fields and the  $\text{XCO}_2$  2D field (Fig. 3c) (as computed from the CHIMERE 3D fields, see section 2.6.1) reveal the fine scale patterns associated to the anthropogenic emissions (with a strong negative amplitude up to  $-10$  ppm  $\%$  in the  $^{14}\text{CO}_2$  field) and larger scale variations associated to biogenic fluxes and diffuse emissions.

The  $^{14}\text{CO}_2$  field also shows the positive signature from the nuclear emissions and, in particular, the plume from La Hague nuclear reprocessing plan with large values, which can exceed 80 ppm %.

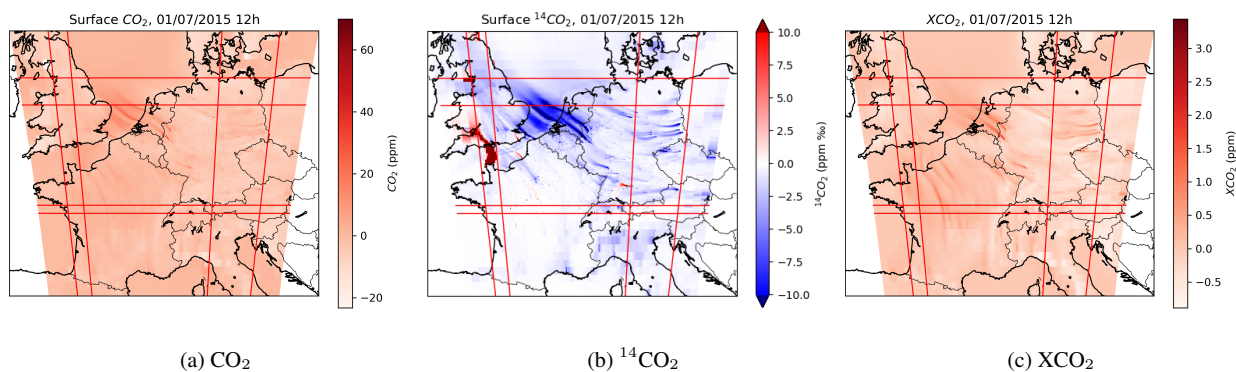


**Figure 3.**  $\text{CO}_2$  (ppm) and  $^{14}\text{CO}_2$  (ppm %) mole fractions at the surface and  $\text{XCO}_2$  (ppm) at 12:00, on July 1 2015: simulations from 00:00 to 12:00, without initial and boundary conditions.

## 330 2.5 Control Vector

### 2.5.1 Definition of the Control Vector

The control vector is spatialized based on a decomposition of the flux maps into large or administrative regions, large urban areas and large industrial plants.

The study focuses on a set of 23 regions, called “the main area of interest” hereafter: the nine administrative regions of  
 335 Belgium, Luxemburg, seven administrative regions of the southern Netherlands, three administrative regions in northern France and three administrative regions in western Germany (all comprised in the  $2 \text{ km} \times 2 \text{ km}$ -resolution zoom of the CHIMERE grid, see Fig.Figure 4).

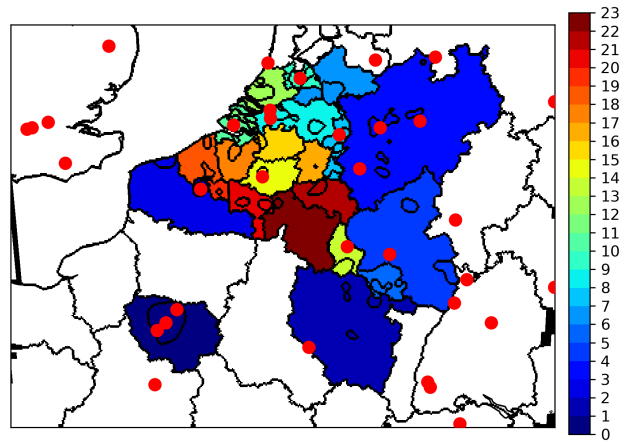


**Figure 4.** Main area of interest i.e. the 23 administrative regions where major urban areas (contours of the urban areas also represented here) and point sources emissions are controlled separately for anthropogenic emissions in the  $2\text{ km} \times 2\text{ km}$ -resolution zoom of the CHIMERE transport model. The names of these administrative regions are listed in Table 1. Ground-based  $^{14}\text{CO}_2$  and  $\text{CO}_2$  observation sites are also shown (red dots, see Fig. 7, for the network on the whole domain).

**Table 1.** List of areas of control in the main area of interest and corresponding number of stations in these areas.

Number	Area Name	Number of Stations
1	Île-de-France	3
2	Lorraine	1
3	Nord-Pas-de-Calais	1
4	North Rhine Westphalia	3
5	Rhineland-Palatinate	1
6	Saarland	0
7	Gelderland	0
8	Limburg	1
9	North Brabant	3
10	Utrecht	1
11	Zeeland	1
12	Sheldt (see)	0
13	South Holland	0
14	Luxemburg	1
15	Brabant/Bruxelles	1
16	Anvers	0
17	Limburg	0
18	East Flanders	0
19	West Flanders	0
20	West Hainaut	0
21	East Hainaut	0
22	Liege	0
23	Namur/Luxembourg	0

In this main area of interest, the CO<sub>2</sub> FF emission budgets from major industrial plants (22 plants for which the annual emissions exceed 1 MtC for CO<sub>2</sub>, FF<sub>PS</sub>, see the red dots in Fig. Figure 4) and the FF, BF<sub>wood</sub> and BF<sub>crop</sub> CO<sub>2</sub> emission budgets from the large urban areas (the 42 urban areas represented in Fig. Figure 4) are controlled separately. In each of these 23 regions, the budget of the rest of the FF, BF<sub>wood</sub> and BF<sub>crop</sub> CO<sub>2</sub> emissions are controlled separately. Outside this main area of interest, the FF, BF<sub>wood</sub> and BF<sub>crop</sub> CO<sub>2</sub> emission budgets of 43 administrative or larger regions are controlled (Fig. 5).

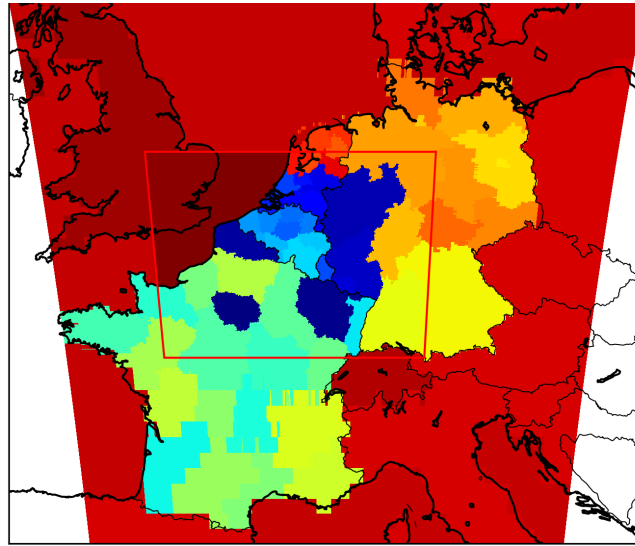


**Figure 5.** Administrative regions and coarser areas for which the biogenic flux budgets, and the anthropogenic emission budgets (with more details for regions highlighted in Fig. Figure 4) are controlled. The red line delimits the  $2 \text{ km} \times 2 \text{ km}$ -resolution zoom of the CHIMERE transport model.

Single  $^{14}\text{C}$  signatures of the  $\text{BF}_{wood}$  and  $\text{BF}_{crop}$  fluxes are controlled assuming that they apply over the whole modelling domain. The  $^{14}\text{C}$  fluxes from 47 nuclear power plants, across the whole modeling domain, are separately controlled.

Biogenic fluxes and isotopic signatures (NPP, HR and  $\delta_{HR}$ ) are only controlled at the resolution of the 66 administrative regions and larger areas (23 in the main area of interest and 42 outside, Fig. 5), i.e., the spatial resolution of the control vector is nearly the same as for anthropogenic emissions but it does not isolate urban areas and major point sources.

The control vector is actually composed of scaling factors to be applied to maps of local (from plant and urban area) and regional fluxes from the products presented in Section 2.3 over these spatial control areas at a 1-hour temporal resolution except for the  $^{14}\text{C}$  signature of the HR, of wood burning and of crops BF emissions which are controlled at the daily scale. **Indeed, anthropogenic emissions and biogenic fluxes of  $\text{CO}_2$  can have a high temporal variability at the hourly scale. While the product used to define the component of  $\mathbf{H}_{distr}$  corresponding to nuclear emissions is based on annual values (see Section 2.3), the actual nuclear emissions can vary a lot at fine temporal scales (studies such as that of Cany et al. (2018) show large variations of the nuclear production of individual sites, and the emissions may actually be primarily driven by maintenance processes).** The composition of the control vector is summarized in Table 2.



**Table 2.** Number of parameters in the control vector. The control vector is composed of scaling factors to be applied to budgets and maps of local and regional fluxes from the products presented in Section 2.3 ( $FF_{PS}$ ,  $FF_{other}$ ,  $BF_{crop}$ ,  $BF_{wood}$ , NPP, HR,  $^{14}C_{BF_{crop}}$ ,  $^{14}C_{BF_{wood}}$ ,  $^{14}C_{HR}$  and Nucl). This table gives number and type of areas in the control vector: 66 administrative or coarser regions (Reg) defined in [Fig. Figure 5](#) and more detailed areas in the main area of interest. PS: point source emissions, UA: large urban area emissions, NUA: non urban area i.e the rest of the region when excluding the UA and Domain: whole domain budget. In a 24h-inversion-window, 24 temporal parameters correspond to 1h temporal resolution and 1 parameter correspond to daily resolution.

		$FF_{PS}$	$FF_{other}$	$BF_{crop}$	$BF_{wood}$	NPP	HR	$^{14}C_{BF_{crop}}$	$^{14}C_{BF_{wood}}$	$^{14}C_{HR}$	$F_{Nucl}$
Spatial	in Main Area of Interest	22 PS -	42 UA 23 NUA	42 UA 23 NUA	42 UA 23 NUA	66 Reg	66 Reg	1 Domain	1 Domain	66 Reg	47 PS
	outside		43 Reg	43 Reg	43 Reg						
	Total	22	108	108	108	66	66	1	1	66	47
Temporal		24	24	24	24	24	24	1	1	1	24
Total		528	2592	2592	2592	1584	1584	1	1	66	1128
<b>Control Vector Size</b>		<b>126681428</b>									

### 2.5.2 Prior error covariance matrix **B**

**B** is built assuming a 3-hour temporal auto-correlation of the prior uncertainty in hourly budgets for each type of controlled flux. An exponentially decaying function is used to model these temporal correlations:  $e^{-d/3}$ , where d is the time lag, expressed in hours, between two hourly fluxes. We also assume that there is no correlation of the prior uncertainties in space (between different point sources, urban areas and regions) or between different types of fluxes or isotopic signatures. The standard deviations of the prior uncertainties in control parameters for individual spatial areas at daily scale are set to 30% for FF and BF emissions, to 100% for  $^{14}C$  signatures and to 60% for biogenic fluxes (Table 3). The resulting standard deviations of prior uncertainty in regional 24-h, morning and afternoon budgets of FF emissions in the main area of interest range from 10 to 45% (Table 4). Hereafter, when analysing uncertainties in temporal budgets of fluxes, “morning” and “afternoon” are used to designate the time windows 6:00-13:00 and 13:00-19:00 UTC, respectively.

**Table 3.** Standard deviations of the prior uncertainties in 24-h budgets of controlled fluxes or in controlled isotopic signatures for each control area.

	$FF_{PS}$	$FF_{other}$	$BF_{crop}$	$BF_{wood}$	NPP	HR	$^{14}C_{BF_{crop}}$	$^{14}C_{BF_{wood}}$	$^{14}C_{HR}$	Nucl
Prior uncertainty (%)	30	30	30	30	60	60	100	100	100	100

**Table 4.** Range of standard deviations of the prior uncertainty in regional 24-h, morning and afternoon budgets of FF emissions in the main area of interest. These budgets include the urban areas and point sources within the regions

Prior uncertainty in regional budget (%)	24-h	Morning	Afternoon
Min	10	15	16
Mean	20	29	31
Max	30	43	45

## 2.6 Observation vector and corresponding sets of experiments

### 2.6.1 Satellite observations from an XCO<sub>2</sub> spectral imager similar to CO2M

Some of the experiments assimilate pseudo retrievals of XCO<sub>2</sub> from a single orbit of a CO2M-like satellite passing over Western Europe at 12:00 UTC. The simulation of these XCO<sub>2</sub> satellite observations is based on the simulations of the CO2M 2-km-resolution sampling, with a ~300 km swath, and L2 error statistics in the surface and atmospheric conditions for the year 2014 from the ESA-PMIF project (Wang et al., 2020; Lespinas et al., 2020). These simulations account for cloud cover which is moderate for the selected orbit (Fig. Figure 6). The observation vector is defined by the individual cloud free pixels of the satellite. The extraction of this observation vector from the model outputs is made by selecting the model grid cells in which the centres of these pixels are located. The spatial resolution of our transport model in the area of interest is similar to that of the satellite observation. However, since the satellite ground pixels do not perfectly correspond to the model grid cells in this area, some model grid cells can correspond to several observations. In the coarser part of the model grid, model grid cells correspond to several observations.

XCO<sub>2</sub> is computed from the CHIMERE 3D fields of CO<sub>2</sub> following the rationale of Santaren et al. (2021), notably assuming a constant vertical weighting function:

$$X_{CO_2}(lat, lon) = \frac{\overline{CO_2(P_{top})} \times P_{top} + \int_{P_{top}}^{P_{surf}(lat, lon)} (CO_2(lat, lon, P) \times dP)}{P_{surf}(lat, lon)} \quad (7)$$

where *lat* and *lon* are the latitude and the longitude, respectively, *P* is the atmospheric pressure. *P<sub>surf</sub>* is the surface pressure and *P<sub>top</sub>* (300 hPa) is the pressure at the top boundary of the model. For pressures lower than *P<sub>top</sub>*, we assume that the CO<sub>2</sub> mole fraction concentration equal the horizontal average of the top-level mixing ratios in CHIMERE ( $\overline{CO_2(P_{top})}$ ).

### 2.6.2 Ground-based network

We use a surface network (Fig. 7) of which 113 stations in our modelling domain are located following the scenario proposed by Marshall et al. (2019). This scenario is based on existing continuous CO<sub>2</sub> measurement sites of the Integrated Carbon Observation System (ICOS, <https://www.icos-cp.eu/>), other air sampling stations of the National Oceanic and Atmospheric Administration (NOAA) and of the Global Atmosphere Watch Programme of World Meteorological Organization (GAW,

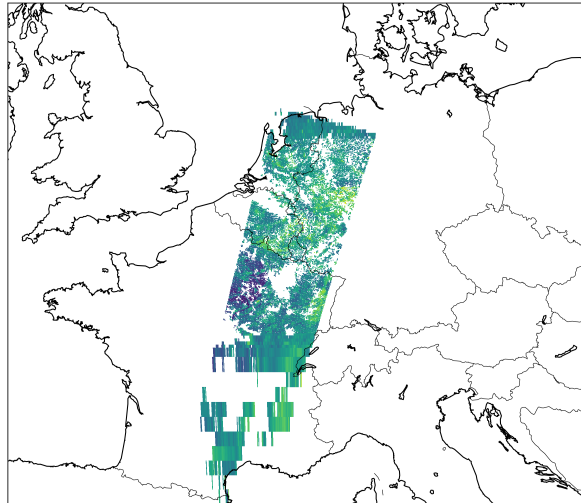


**Figure 6.** Simulation of the XCO<sub>2</sub> sampling and observation error standard deviation (by IUPB in the ESA-PMIF project) for a selected orbit of the spectral imaging satellite, in parts per million (ppm).

390 <https://community.wmo.int/activity-areas/gaw>), but also local meteorological or air quality sampling stations and local science and engineering faculties. We assume that these stations have appropriate infrastructures and locations to observe atmospheric CO<sub>2</sub> and <sup>14</sup>CO<sub>2</sub>. ~~In order to complement this first network, local meteorological or air quality sampling stations, or local science and engineering faculties were also chosen.~~

The sampling height at these stations ranges between 10 and 344 m above the ground level. We assume that all stations  
 395 of this network measure simultaneously CO<sub>2</sub> and/or <sup>14</sup>CO<sub>2</sub>. ~~In order to simplify the pseudo-data framework and since the main area of interest has a relatively low and flat topography, e~~Each virtual site is assumed to provide hourly CO<sub>2</sub> data that are suitably assimilated between 10:00 and 17:00 UTC and/or a 7-hour-average sample of <sup>14</sup>CO<sub>2</sub> over 10:00-17:00 UTC, following the common practice of assimilating data from low-altitude stations only when the planetary boundary layer (PBL) is well developed (Broquet et al., 2011; Monteil et al., 2020; Munassar et al., 2022)~~(Broquet et al., 2011)~~. The availability of  
 400 CO<sub>2</sub> 7-hour averages when deriving <sup>14</sup>CO<sub>2</sub> 7-hour averages from air samples is ignored.

### 2.6.3 Observation error covariance matrix **R**

The matrix **R** combines the uncertainty in the data that are assimilated and the corresponding uncertainty from the observation operator. Here we assume that the uncertainty in the observation operator is dominated by that of the transport model and we ignore temporal and spatial auto-correlations in these uncertainties. ~~The representation and aggregation errors associated to~~

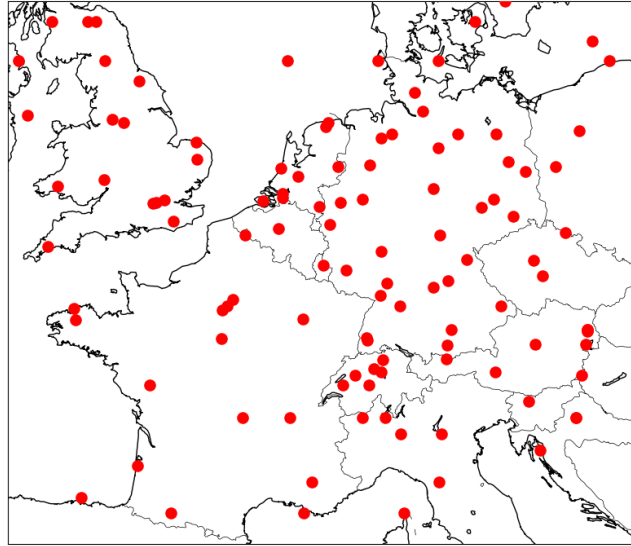


**Figure 7.** Ground-based  $^{14}\text{CO}_2$  and  $\text{CO}_2$  observation networks. 113 stations located following the scenario proposed by Marshall et al. (2019), based on real or potential observation networks (ICOS, NOAA, GAW, more details in section 2.6.2).

405 the spatial and temporal resolutions of the transport model and control vector (Kaminski et al., 2001; Wang et al., 2017) are assumed to be small in the main area of interest since these resolutions are relatively high for this area in our inverse modeling framework. They are neglected over the whole domain. For individual data, the standard deviation of the observation error is therefore:

$$\sigma_{obs} = \sqrt{\sigma_{meas}^2 + \sigma_{mod}^2} \quad (8)$$

410 For satellite observations,  $\sigma_{meas}$  is the uncertainty in the  $\text{CO}_2\text{M XCO}_2$  data as simulated by IUPB. These values are represented in Fig. Figure 6.  $\sigma_{mod}$  is taken as 1 ppm for individual data (Basu et al., 2018; Marshall et al., 2019). As described in Section 2.6, since the satellite ground pixels do not perfectly correspond to the model grid cells, some model grid cells can correspond to several observations. We assume that the observation errors are uncorrelated: the aggregation of  $N$  observations results in decreasing errors by a factor  $1/\sqrt{N}$ .

415

For the near surface  $\text{CO}_2$  and  $^{14}\text{CO}_2$  observations, the configuration of  $\sigma_{meas}$  follows the guidelines of Marshall et al. (2019, Tables 5-1 to 5-3):

- The uncertainty in  $\text{CO}_2$  hourly measurements is taken as the target measurement uncertainty,  $\sigma_{\text{CO}_2,meas} = 0.05$  ppm.

– The 1-sigma uncertainty on  $^{14}\text{CO}_2$  7-hour data is taken as 200 ppm ‰, based on the following uncertainty propagation:

420

$$\sigma_{^{14}\text{CO}_2, meas} = \sqrt{(CO_2 \times \sigma_{\delta^{14}\text{C}, measobs})^2 + (\delta^{14}\text{C}, a \times \sigma_{CO_2, measobs} / \sqrt{7})^2} \quad (9)$$

with

- $\text{CO}_2$  the atmospheric mole fraction concentration set to 400 ppm
- the atmospheric  $\delta^{14}\text{C}, a$  set to 40 ‰
- $\sigma_{CO_2, meas} / \sqrt{7}$ , the  $\text{CO}_2$  measurement uncertainty at the 7-hour scale, assuming that there is no autocorrelation in the  $\text{CO}_2$  measurement errors at the hourly scale
- $\sigma_{\delta^{14}\text{C}, meas} = 0.5\text{‰}$ , the  $\delta^{14}\text{C}$  measurement uncertainty at the 7-hour scale

425

We use the estimate of the model error from Marshall et al. (2019, Tables 5-2 and 5-3):  $\sigma_{CO_2, model} = 1$  ppm and  $\sigma_{^{14}\text{CO}_2, model} = 1.26 \times 10^{-12}$  ppm multiplied by a coefficient ranging between 1 and 5. This coefficient corresponds to the amplitude of the variability of the signal, and to the level of complexity for the transport simulation at the different types of stations: 1.0 for tall towers, 1.5 for mountain sites, 3.0 for continental low altitude stations and 5.0 for sites within urban areas or close to strong sources. For  $^{14}\text{CO}_2$ , the conversion was done from ppm to ppm ‰ by multiplying by 1000/ $R_{std}$ . Ignoring auto correlations in the model error at the hourly scale, the model error for 7-hour  $^{14}\text{CO}_2$  mean mole fraction concentration data is taken as  $1/\sqrt{7}$  times the model error derived at the 1-hour scale.

430

The range of the resulting error statistics on the different types of data and from the model are reported in Table 5.

**Table 5.** Data, model, and observation operator 1-sigma uncertainty

Error	Near-surface			Satellite		
	Meas	Model	Obs	Meas	Model	Obs
$\text{CO}_2$ (ppm)	0.05	1 to 5	1 to 5	0.38 to 0.75	1	1.07 to 1.11
$^{14}\text{CO}_2$ (ppm ‰)	200	405 to 2025	451 to 2034			

#### 435 2.6.4 List of experiments

Table 6 provides labels for the different sets of experiments as a function of the sets of pseudo observations that are assimilated, using or combining the satellite data, the surface  $\text{CO}_2$  data and/or the surface  $^{14}\text{CO}_2$  data. The problem of the attribution of inferred fluxes to FF or BF emissions, to NEE or to nuclear emissions is investigated by conducting sensitivity tests in which the NEE, the BF emissions or the nuclear emissions are ignored, i.e. assuming no uncertainty in these fluxes. For the sake of simplicity, we do not define specific labels for this and the text will clarify whenever diagnostics refer to these tests "without BF emissions, NEE or nuclear emissions".

440

**Table 6.** List of performed experiments

Inversion System Observations	Name
Satellite XCO <sub>2</sub>	INV-SAT
Surface CO <sub>2</sub>	INV-CO <sub>2</sub>
Surface <sup>14</sup> CO <sub>2</sub>	INV-14C
Satellite XCO <sub>2</sub> + Surface CO <sub>2</sub>	INV-SAT-CO <sub>2</sub>
Satellite XCO <sub>2</sub> + Surface <sup>14</sup> CO <sub>2</sub>	INV-SAT-14C
Satellite XCO <sub>2</sub> + Surface CO <sub>2</sub> + Surface <sup>14</sup> CO <sub>2</sub>	INV-SAT-CO <sub>2</sub> -14C

## 2.7 Diagnostics

When analysing the results from the inversions and assessing the potential of the different types of observation networks, we focus on the standard deviation of the prior and posterior uncertainties in flux budgets, and on their relative difference (called uncertainty reduction or UR hereafter):

$$UR = 1 - \frac{\sigma_{post}}{\sigma_{prior}} \quad (10)$$

Hereafter, when analysing temporal budgets of uncertainties, “morning” and “afternoon” are used to designate 6:00-13:00 and 13:00-19:00 UTC, respectively. Our analyses are focused on budgets for regions in the 2-km-resolution area and more particularly in the main area of interest as defined in Figure 4.

To evaluate the impact of ground-based networks, we also define  $\Delta UR_{Test}^{Ref}$  as the difference between UR for 24-h FF regional budgets, with a test configuration and UR with a reference configuration:  $\Delta UR_{Test}^{Ref} = UR_{test} - UR_{Ref}$ . In these cases the reference configurations are the ones when assimilating the data from the satellite track, either alone or with CO<sub>2</sub> data from the ground network (INV-SAT and INV-SAT-CO<sub>2</sub> see Table 6).

## 3 Results

### 3.1 Potential of the satellite observations as a standalone observation system

This section describes results when assimilating the data from the satellite track only, i.e. results from the INV-SAT inversion.

#### 3.1.1 General results in the morning

This section focuses on results on morning budgets for which the constraint in the inversion from the satellite observation is the highest. Indeed, the maximum maximal UR for regional morning budgets reaches 32% against 3% for afternoon budgets (Table 7).

**Table 7.** Best score statistics of the uncertainty reductions (UR max for the highest UR) and the posterior uncertainty (Post min for the smallest posterior uncertainty) in inversions with and without NEE, for regional 24-h, morning and afternoon FF emission regional budgets. In the main area of interest, these budgets combine emissions from urban areas, large plants and the more diffuse regional sources.

		Uncertainties (%)	INV-SAT	INV-CO2	INV-SAT-CO2	INV-14C	INV-SAT-CO2-14C
With NEE	24-h	UR max	18,4	12.6	23,6	23.0	32,9
		Post min	8,0	8.6	7,5	7.6	6,6
	Morning	UR max	32,4	17.7	37,8	32.7	50,8
		Post min	10,0	12.2	9,2	10.0	7,3
	Afternoon	UR max	2,9	14.7	15,8	10.8	20,5
		Post min	15,6	14.9	14,6	15.1	14,0
Without NEE	24-h	UR max	32.2	26.4	39.2	23.4	40.7
		Post min	6.7	7.2	6.0	7.5	5.8
	Morning	UR max	59.9	36.9	64.4	33.3	66.0
		Post min	5.9	9.3	5.3	9.9	5.0
	Afternoon	UR max	3.9	17.0	17.0	10.8	21.2
		Post min	15.5	13.7	13.4	15.1	13.2

Figure 8 shows the example of a panel of URs from INV-SAT, for the morning budget of CO<sub>2</sub> fluxes, at the scale of point sources to that of regions. The URs for the morning budgets of large industrial plant emissions (FF<sub>PS</sub>) are significant in the satellite field of view (FOV, corresponding to the vertical projection of the satellite image on the ground), with values larger than 50% (Fig. 8a), but is marginal outside this FOV. The northwest direction of the wind on the day of analysis (see Section 2.2) explains that the observation footprint appears to be slightly extended out of this FOV, in the east, with, for example, significant UR in the region of Essen. URs are also significant for other fossil fuel emission budgets (FF<sub>other</sub>) and HR (heterotrophic respiration, as defined above) in the satellite FOV with URs up to 50% and more. The UR for NPP is much larger than for the other fluxes. This can be explained by the fact that the level of UR for a given flux is strongly driven by the ratio in the observation space between the imprint of the uncertainty in this flux and that of the uncertainty in the other fluxes added to the observation and transport model errors. The NPP is relatively large in July and thus bears a large absolute uncertainty with a widespread imprint, so that this ratio is high for this flux. ~~since this flux is relatively large in July.~~ The UR for BF emissions is generally much smaller than for the FF emissions. The much weaker level of emission related to BF combustion explains the lack of UR for this type of fluxes.

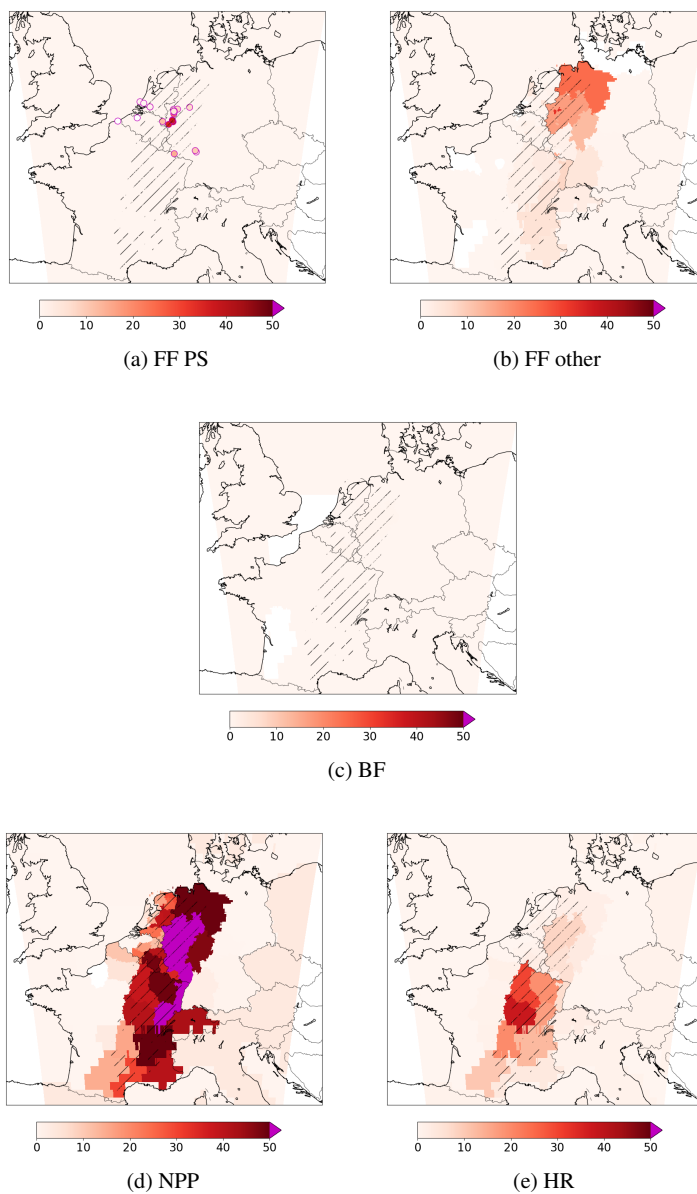


**Figure 8.** Uncertainty reduction in INV-Sat inversions: for morning budgets of large plants (a, FF\_PS, magenta circled dots), other FF (b) and BF (c, crop and wood) emissions (urban area and rest of the region budgets), Net Primary Production (d, NPP) and heterotrophic respiration (e, HR) (regional budgets). Stripes are indicative of the satellite field of view (see Fig. 6 for the full track).



### 3.1.2 Uncertainties in FF emissions

475 The uncertainty reductions for the 24-hour regional budgets of FF emissions (regional budgets aggregates emissions from urban areas, point source and the rest of the regions hereafter) range from 0 to 18% in the main area of interest (Fig. 10, a, [TableTab. 7](#)). The URs are similar or rise in a range from 0 to 32% for the regional morning budget (Fig. 9, a and [TableTab. 7](#)). Larger emission budgets generally lead to larger URs. However, for similar or lower emission budgets (median 8 vs. 14  $kTCO_2 \cdot d^{-1}$   $kTCO_2 \cdot area^{-1} \cdot 24h^{-1}$  respectively), URs are significantly higher for emissions from urban areas than for the other regional  
480 emissions (max 18% vs. 10% respectively) since dense emissions areas generate atmospheric signatures with large amplitudes that are easier to filter from other signatures and from the observation noise than more extended but more diffuse emissions areas (Santaren et al., 2021). URs for the afternoon emissions entirely rely on the specification of 3-h temporal auto-correlation in the prior uncertainties in the emissions since these afternoon emissions are not directly seen by the satellite [in our regional inverse problem with a satellite overpass at 12:00 UTC](#). Consequently, [URsthey](#) are low for all types of sources. Figure 9(b)  
485 and Table 7 show URs for afternoon regional budgets ranging from 0 to 3%. Overall, the results show contrasting capacities for the monitoring of the FF emissions. The scores of URs result in various levels of precision on the emission estimates, with 8% to 30% posterior uncertainties in 24-hour and regional budgets of FF emissions in the main area of interest ([TableTab. 7](#)). The lack of constraint outside the satellite FOV and during periods other than the morning confirms the need for complementary data to extrapolate the information derived from the satellite observations in space and time.

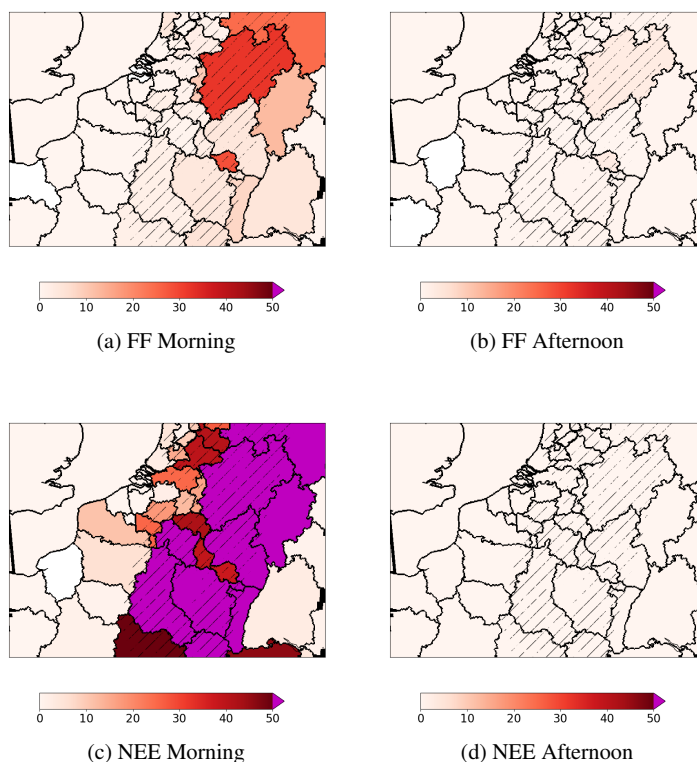


**Figure 9.** Uncertainty reduction in INV-Sat inversion: for morning (a, c) or afternoon (b, d) budgets of FF, biogenic fluxes (NEE). Stripes are indicative of the satellite field of view (see Fig. 6 for the full track).

### 490 3.1.3 Impact of NEE and BF emissions on FF emissions uncertainties

The UR for NEE is much larger than for the FF emissions (Fig. 9, b and c) while the UR for BF emissions is generally much smaller than for the FF emissions (Fig. 8). The problem of the attribution of inferred fluxes to FF emissions, NEE or BF emissions is investigated [with theby conducting](#) sensitivity tests in which the NEE or BF emissions are ignored, *i.e. assuming no uncertainty in these fluxes* (results when ignoring BF emissions are not shown in the figures and tables for the reasons given below). The INV-SAT experiment ignoring the NEE shows significantly larger URs for the FF regional 24-h budgets (Fig. [Figure 10](#)), up to 60% in the satellite FOV, for the FF regional morning budget (Table 7, without NEE). This increase of the URs yields posterior uncertainties in 24-h regional budgets which can reach values as low as 6.7% in the satellite FOV ([Table Tab. 7](#)).

## INV-Sat 24-h FF budget

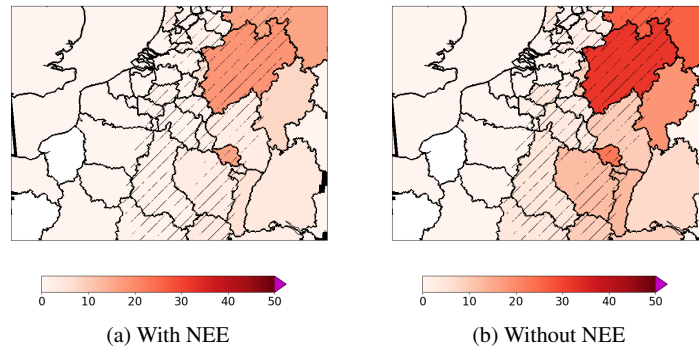


**Figure 10.** Uncertainty reduction in INV-Sat inversion with (a) and without (b) NEE, for 24-h budgets of FF emissions. Stripes are indicative of the satellite field of view (see Fig. 6 for the full track).

The sensitivity of the INV-SAT experiment to the inclusion of BF emissions shows a very weak impact of BF emissions on the UR for FF emissions (not shown) even though the spatial distribution of these two types of emissions are strongly correlated. This is directly attributed to the weak amplitude of BF emissions compared to FF emissions. Typically, the posterior uncertainty in the FF emissions (6 to 30 % of the 24-h BF + FF emission budget) is much larger than the prior uncertainty in BF emissions (0 to 7% of the 24-h BF + FF emission budget).

### 3.2 Potential of the ground-based hourly CO<sub>2</sub> network

This section evaluates the impact of co-assimilating data from the ground-based hourly CO<sub>2</sub> network and the potential complementarity between the satellite and the CO<sub>2</sub> ground-based hourly observations. This evaluation is based on the analysis of INV-CO<sub>2</sub> and INV-SAT-CO<sub>2</sub> and comparisons with the results from INV-SAT.

#### 3.2.1 General results for the FF emissions

INV-CO<sub>2</sub> (Fig. 11) reveals the limited role of the horizontal atmospheric transport near the surface to propagate URs from regions with several measurement stations to other regions. URs of more than 4%, median at 12% and maximum at 13%, for 24-h budgets can be achieved in regions with 3 stations, like Île-de-France (Reg. 1, 12%), and North Rhine-Westphalia (Reg.4, 13%) in the main area of interest (see also Fig. A1), or in regions with more stations outside this area like southeast England (10%) and Baden-Württemberg (26%) which have 5 stations. However, the UR can also be much lower in regions with many stations, e.g. for Lower-Saxony-and-Bremen which has 5 stations but a 4% UR. UR in regions with 1 or 2 stations

515 range between 0% and 6%. The URs are generally below 1% for other regions. These URs reach lower or comparable values than in the INV-SAT experiment in the main area of interest (Fig.A1, Tab 7). However, outside the main area of interest, Baden-Württemberg reaches a higher value than the largest one with the INV-SAT experiment (Rhineland-Palatinate, Reg. 5, 18%).

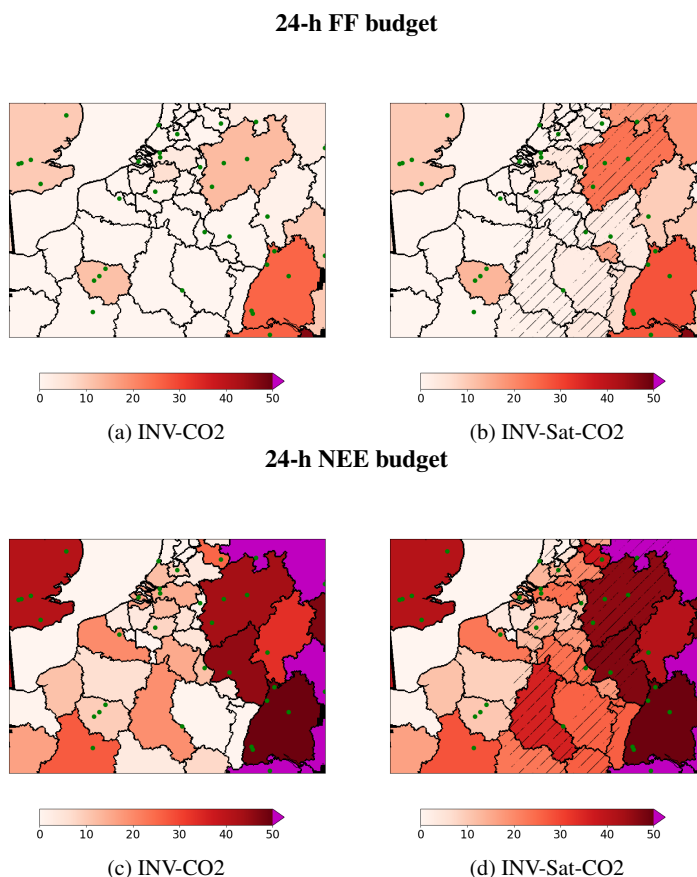


**Figure 11.** Uncertainty reduction in INV-CO<sub>2</sub> (a, c) and INV-Sat-CO<sub>2</sub> (b, d) inversions: for 24-h budgets of FF emissions and biogenic fluxes (NEE). Stripes are indicative of the satellite field of view. Green dots indicate the ground stations.

Of note is that the highest UR in the whole inversion domain (47% for 24-hour budgets and 56% for morning budgets) corresponds to large regions of the coarse resolution area of the transport model (not represented in Fig. 11). This result is primarily driven by the **optimistic** extrapolation of information from the sites to the coarse model grid cells and further to the whole extent of the control areas in which they stand, **which is suitable here because of the optimistic lack of account for the representation and aggregation errors impact observations in the coarse resolution part of the transport and inverse modeling domains (see section 2.6).** This optimistic bias from the inversion configuration **would** actually results in representation and

520

525 aggregation errors when conducting experiments with real data (Kaminski et al., 2001) (Wang et al., 2017). The difficulty to  
 characterize these errors (Wang et al., 2017) justifies and supports the use of the finer resolution control vector in the main  
 area of interest, and the focus of our analysis on the 2-km resolution model subdomain. Unlike satellite data alone in INV-SAT,  
 the ground-based CO<sub>2</sub> data constrains both afternoon and morning emission estimates, with URs of 4 to 18% and 4 to 15%  
 530 respectively for morning and afternoon regional budgets of FF emissions in the regions with 3 or more stations (Fig. A3 and  
 A4).

### 3.2.2 Co-assimilation of the satellite observations

Only one region of the 2-km resolution model subdomain with 3 stations is located in the satellite FOV: North Rhine-  
 Westphalia. When comparing the URs for the 24-h regional budgets of FF emissions from INV-SAT-CO2 to that from INV-SAT  
 and INV-CO2 (Table 8, Fig. A1) two significant changes can be seen. The first one is the decrease of 5% of the posterior  
 535 uncertainty for this region, i.e. less than the UR for this region in INV-CO2 (12%). The second one is the increase of UR for  
 the regions outside the satellite FOV with more than 3 ground-based stations from nearly 0% to values that are nearly the  
 same as in INV-CO2. The URs at 24-h scale in INV-SAT-CO2 are smaller than the addition of URs in INV-SAT and INV-CO2  
 experiment (Fig. 12 and Fig. A1)

**Table 8.** CO<sub>2</sub> or/and <sup>14</sup>CO<sub>2</sub> ground network impact in addition to satellite observation:  $\Delta UR_{Test}^{Ref}$  on 24-h, Morning and Afternoon FF re-  
 gional budgets, Maximal value on the AOI (column MAX), and value of the 2 most impacted area (Île-de-France and North Rhine Westphalia,  
 column).

	Test	Ref	$\Delta UR_{Test}^{Ref} (\%)$			
			MAX	MEAN	Île-de-France	North Rhine Westphalia
Daily	INV-SAT-CO2	INV-SAT	13,3	1,6	13,3	5,2
	INV-SAT-14C	INV-SAT	14,6	2,5	14,6	12,7
	INV-SAT-CO2-14C	INV-SAT	20,8	3,3	20,8	14,5
	INV-SAT-CO2-14C	INV-SAT-CO2	9,3	1,8	7,5	9,3
Morning	INV-SAT-CO2	INV-SAT	12,7	1,7	12,7	5,4
	INV-SAT-14C	INV-SAT	16,5	2,7	11,9	16,5
	INV-SAT-CO2-14C	INV-SAT	19,2	3,7	19,2	18,4
	INV-SAT-CO2-14C	INV-SAT-CO2	13	2,1	6,5	13
Afternoon	INV-SAT-CO2	INV-SAT	15,8	1,2	15,8	6,4
	INV-SAT-14C	INV-SAT	10,8	1	10,8	5,6
	INV-SAT-CO2-14C	INV-SAT	20,5	1,8	20,5	10
	INV-SAT-CO2-14C	INV-SAT-CO2	4,7	0,5	4,7	3,6

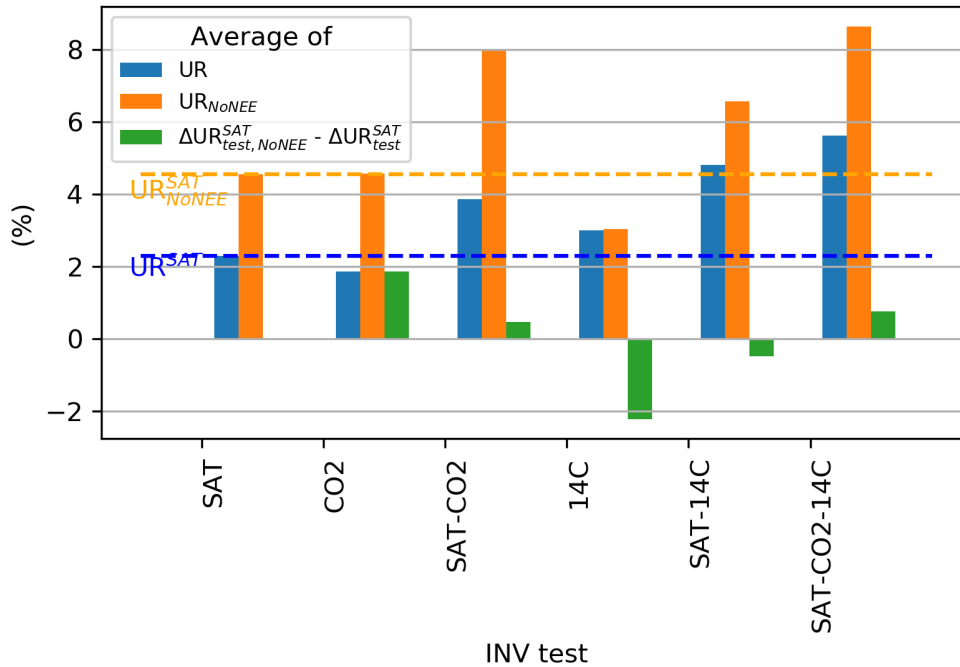


**Figure 12.** Average on the main area of interest of the UR on 24-h FF regional budgets in a set of inversion configurations, with (blue) and without (orange) NEE and average of the difference between  $\Delta UR_{test}^{SAT}$  with and without NEE (green). Negative values highlight an increase of the additional observation network potential when NEE is taken into account. Positive values highlight a decrease of the additional observation network potential when NEE is taken into account. High absolute values highlight strong NEE impact.

The ground-based CO<sub>2</sub> data constrains both afternoon and morning emission estimates, with URs of 3 to 30% and of 1 to 27% respectively for morning and afternoon regional budgets of FF emissions in the regions with three or more stations (data not shown). The comparison between results for afternoon budgets of the FF emissions from INV-SAT-CO2 and INV-SAT shows again, in INV-SAT-CO2, an increased UR that is smaller than the sum of the URs obtained in INV-SAT and INV-CO2 (Table 7). Combining the satellite data with the afternoon data from the ground network does not increase the ability to extrapolate the spatially widely spread information from these satellite data to the afternoon.

### 545 3.2.3 Impact of NEE and BF emissions on FF emissions uncertainty

INV-CO<sub>2</sub> and the results of INV-SAT-CO<sub>2</sub> outside the FOV of the satellite show different situations regarding the comparison between UR for NEE and FF emissions (Fig. 11). In regions with large cities and industrial plants (like the Paris area and Baden-Württemberg), the URs for NEE are smaller than ~~that~~ for FF as in INV-SAT. However, in other regions, the signal at the surface stations is dominated by the signature of the biogenic fluxes and URs for NEE are larger than ~~that~~ for FF emissions. 550 Due to the relatively weak signal from BF emissions, the URs for these emissions are much smaller than ~~that~~ for FF emissions (less than 3%, less than 0.1% on average) in INV-CO<sub>2</sub>.

The impact of the attribution problem when using the surface CO<sub>2</sub> network is quantified, here again, by conducting sensitivity tests in which NEE is ignored (Fig. 12 and ~~TableTab.~~ 7). As the surface network has many stations mostly sensitive to the NEE signal, it is expected to support the distinction between NEE and FF emissions in the inversion, even if the stations measure 555 CO<sub>2</sub> only. In inversions INV-CO<sub>2</sub>, the UR for FF emissions is higher when ignoring the NEE, reaching a range between 18 and 46% for 24-h budgets in the regions with more than 3 stations. However, the comparison between results from INV-SAT-CO<sub>2</sub> and INV-SAT when ignoring these fluxes hardly demonstrates a potential of the surface CO<sub>2</sub> network to reduce the problem of attribution between FF emissions and other fluxes (Fig. 12). Figures 12 show  $\Delta UR_{SAT-CO_2, NoNEE}^{SAT}$  larger than  $\Delta UR_{SAT-CO_2}^{SAT}$  on average, i.e adding the CO<sub>2</sub> network when ignoring the NEE yields a larger increase of the UR than when 560 accounting for NEE. This is linked to the smaller UR associated with CO<sub>2</sub> data when accounting for NEE. There is a lack of indirect feedback on the UR for FF emissions from the lowering of uncertainties in NEE when complementing the satellite data with CO<sub>2</sub> data. However the results for each area taken independently show somewhat contrasting results (Fig. 13) with  $\Delta UR_{SAT-CO_2, NoNEE}^{SAT}$  lower than  $\Delta UR_{SAT-CO_2}^{SAT}$  in some regions.

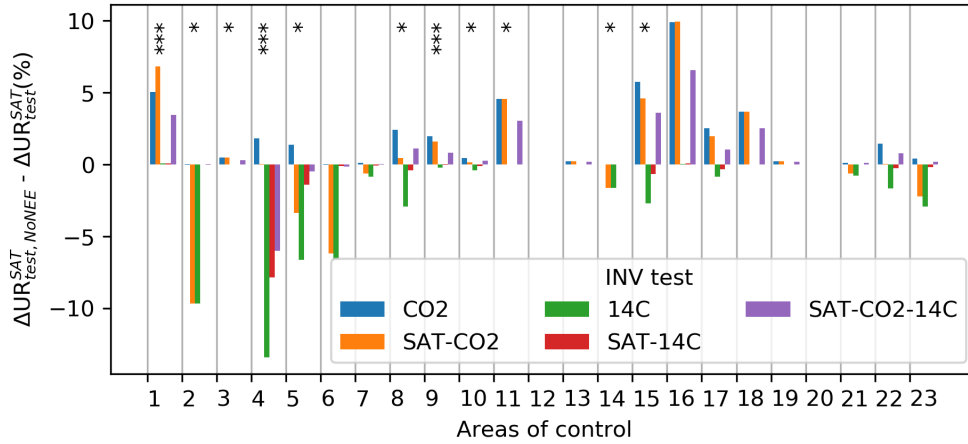


**Figure 13.** Impact of the NEE on the ground network capability on the top of the satellite observation for each area of control in the main area of interest: differences between  $\Delta UR_{test}^{SAT}$  on 24-h FF regional budgets, with and without NEE. Negative values highlight an increase of the additional observation network potential when NEE is taken into account. Positive values highlight a decrease of the additional observation network potential when NEE is taken into account. High absolute values highlight strong NEE impact. The number of stars indicates the number of stations in each controlled area. The areas are listed in Appendix 1.

Regarding BF emissions, the results are similar to that described in section 3.1, i.e a very weak impact of BF emissions on the UR for FF emissions. With INV-SAT-CO2 the posterior uncertainties in FF emissions (7 to 30% of the 24-h BF + FF emission budget) are much larger than the prior uncertainty in BF emissions (0 to 7% of the 24-h BF + FF emission budget).

### 3.3 Potential of the ground-based $^{14}\text{CO}_2$ network

This section evaluates the impact of co-assimilating data from the ground-based 7-h-average  $^{14}\text{CO}_2$  network and the potential complementarities between the satellite and hourly- $\text{CO}_2$ , 7-h-average  $^{14}\text{CO}_2$  ground-based observations. This evaluation is based on the analysis of INV-14C and INV-SAT-CO2-14C and comparisons with the results from INV-CO2 and INV-SAT-CO2.

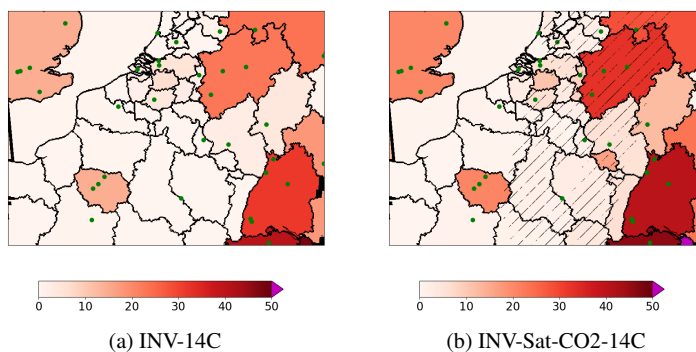
#### 3.3.1 General results for the FF emissions

The spatial distribution of the regional URs for 24-h, morning or afternoon budgets when using surface 7-h-average  $^{14}\text{CO}_2$  data alone is similar to that when using hourly- $\text{CO}_2$  surface data only (Fig. 14). These URs are very low for regions with less than 2 stations (<7%) and range between 12 to 34% for the morning budgets and between 4 to 14% for the afternoon



budgets for regions with more than 3 sites. The URs on daily and morning budgets are larger in INV-14C (TableTab. 7, Fig. A2 and A5), i.e. when using the sampling of  $^{14}\text{CO}_2$  representative of 7-h-averages of the mole fraction concentrations, than in INV-CO2 (TableTab. 7, Fig. A1 and A3), when using 7 hourly  $\text{CO}_2$  data at each site. However, the URs on afternoon budgets are smaller in INV-14C than in INV-CO2. In most regions these differences remain relatively small except in Region 4, North Rhine Westphalia, with up to 15 percentage points difference from the morning budget. The higher potential of  $^{14}\text{CO}_2$  data (7-hour averages) than hourly  $\text{CO}_2$  data to filter the signal from FF emissions, if both were measured at the same temporal resolution, is balanced by the finer temporal resolution of the hourly  $\text{CO}_2$  continuous measurements. The hourly  $\text{CO}_2$  data's finer temporal resolution helps capture the high frequency patterns of the signal from FF emissions.

### 24-h FF budget



### 24-h NEE budget

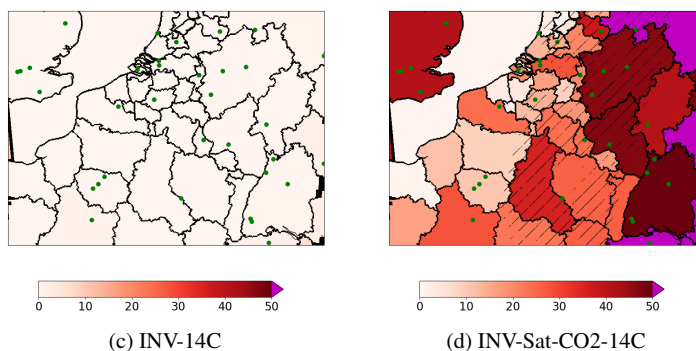


**Figure 14.** Uncertainty reduction in INV-14C (a) and INV-Sat-CO2-14C (c) inversions: for 24-h budgets of FF emissions (a, b, c) and biogenic fluxes (NEE, d, e, f). Stripes are indicative of the satellite field of view (see Fig. 6 for the full track). Green dots indicate the ground stations.

### 3.3.2 Co-assimilation of the satellite and surface hourly-CO<sub>2</sub> observations

585 The fact that the URs when combining two networks is smaller than the sum of the URs when using each of these networks shown when comparing INV-SAT, INV-CO<sub>2</sub> and INV-SAT-CO<sub>2</sub>, also applies when adding the surface network i.e. when comparing e.g. INV-SAT-14C to INV-SAT and INV-14C or INV-SAT-CO<sub>2</sub>-14C to INV-SAT-CO<sub>2</sub> and INV-14C. The combination of 7-h-average <sup>14</sup>CO<sub>2</sub> data with other types of data does not lead to further synergies of the advantages for each network: the spatial extent of the satellite observation, the temporal coverage of the ground-based networks, the temporal resolution of the  
590 hourly-CO<sub>2</sub> surface network, and the higher sensitivity to FF emissions of the 7-h-average <sup>14</sup>CO<sub>2</sub> network. In North Rhine-Westphalia, where the configuration is favourable, with 3 stations in the satellite FOV, the UR for the daily budget increases from 18% with INV-SAT to 33% with INV-SAT-CO<sub>2</sub>-14C (Fig. 14, Reg. 4). This configuration leads to 6.6% posterior uncertainty. In Île-de-France (Reg. 1) outside the satellite FOV and with 3 stations, the UR reaches 21% in INV-SAT-CO<sub>2</sub>-14C, reaching 18% posterior uncertainty. In Saarland (Reg. 6), in the satellite FOV and without stations, the UR remains similar in  
595 INV-SAT-CO<sub>2</sub>-14C as in INV-SAT, 17%, corresponding to 15% posterior uncertainty.

### 3.3.3 Impact of <sup>14</sup>CO<sub>2</sub> sources: nuclear emissions, NEE and BF emissions

The impact of nuclear emissions in the inversions assimilating <sup>14</sup>CO<sub>2</sub> data is analysed by conducting experiments where these emissions are ignored. The comparison of INV-14C experiments with and without nuclear emissions shows a decrease of the URs, in the range of 0-1.7 percentage points (Fig. A7, a), when these 14C emissions are taken into account. In the main area of  
600 interest, the most impacted areas are the Zeeland, Brabant/Bruxelles, Anvers and Flanders regions where the stations are close to nuclear power plants (Fig. A7, b). Outside the main area of interest, Baden-Wurttemberg is also strongly impacted, with up to 9% points difference.

Concerning the impact of NEE, in INV-14C, the URs for FF emissions in the regions with more than 3 stations are higher when ignoring the NEE, reaching a range between 15 and 33% for 24-h budgets. The comparison of the experiments INV-14C  
605 with and without NEE shows a much smaller impact of NEE on the URs for FF emissions than in experiments INV-CO<sub>2</sub> or INV-SAT, which confirms the much smaller sensitivity of <sup>14</sup>CO<sub>2</sub> data to NEE than CO<sub>2</sub> data. An interesting consequence is that, on average,  $\Delta UR_{14C}^{SAT}$ ,  $\Delta UR_{SAT-14C}^{SAT}$  (Fig. 12) or  $\Delta UR_{SAT-CO_2-14C}^{SAT-CO_2}$  (not shown) are slightly larger when accounting for the NEE than when ignoring them. The potential of the <sup>14</sup>CO<sub>2</sub> network to complement the satellite observation is higher when NEE is accounted for, while section 3.2 showed more contrasting results for the surface CO<sub>2</sub> network. This increase of  
610 the impact of the <sup>14</sup>CO<sub>2</sub> network when accounting for NEE is however relatively small, reaching its maximum in the region North Rhine-Westphalia, which has 3 stations, and where the posterior uncertainty decrease for the 24-h regional budgets of FF emissions from INV-SAT to INV-SAT-14C is 15%.

## 4 Discussion and Conclusions

### 4.1 Configuration of the inversion

615 Several caveats should be raised for the interpretation of these results. Part of the lack of amplification of the impact from the different observation subsystems when combining them could be due to our set-up of the prior uncertainties in which we ignore spatial correlations and assume that the temporal correlations are relatively low. These assumptions are conservative and, we believe, safer, in a context where the correlations of uncertainties in current inventories are still poorly characterized and, since they are probably highly complex and far from isotropic, homogeneous, decreasing with distance or time. For 620 instance, distant plants or cities can have more similar processes than **emitters that are spatially near to each other**~~lose ones~~, and the emissions and their underlying processes can vary rapidly depending on the time, weather, or socio-economic drivers. ~~---~~ Inversions assuming large temporal and spatial correlations in the prior uncertainties in inventories would indicate a stronger ability to extrapolate the information from atmospheric data but would be overly optimistic.

The control of the diffuse anthropogenic emissions and natural fluxes at the regional scale, rather than at the spatial resolution 625 of the transport model, allowed for solving for Eq. 1 analytically, but its impact on the results could be questioned. However, the size of the control regions is quite small. Furthermore, the control of such diffuse fluxes is traditionally handled by assigning isotropic spatial correlations to the prior uncertainty in these fluxes. When considering the fluxes at high spatial resolution, this can hardly better correspond to actual errors than the partition among administrative regions, at least for the anthropogenic emissions (as highlighted above).

630 The study focuses on the assessment of the potential and limitation of the observation samplings, but random transport model error statistics are assigned in order to reflect the respective weight of these errors on in situ and satellite data. The specific values attributed to these statistics would directly impact the scores of posterior uncertainty and of URs. However, we assume that the ratio of transport model error statistics between the different types of observations appropriately reflects modeling skills to simulate in situ or satellite data (Marshall et al., 2019) so that the comparison of the scores of URs from the assimilation of 635 different subsets of observations is meaningful. Furthermore, the specific values given to the error statistics, within a realistic range, should not impact the more qualitative insights brought by our analysis, regarding the spatial and temporal coverage of the information on the fluxes provided by the different types of observation networks and regarding the attribution problem.

When using real data, the actual precision of the flux estimates would be strongly impacted by atmospheric radiative transfer and transport modeling uncertainties (Schuh et al., 2019; Crowell et al., 2019). Our model of the uncertainty in the atmo- 640 spheric transport is relatively simple here: a Gaussian distribution without any spatial and temporal correlation in the observation space of the inversion problem, as traditionally done in atmospheric inversions (Peiro et al., 2022; Crowell et al., 2019)(Santaren et al., 2021). Complex modelling errors could actually shift or modify the patterns of the atmospheric signature of the FF emissions, which could increase the weight of the attribution problem, and thus the potential of the combination between satellite and surface data. However, very dense surface networks would be needed to support the identification and 645 adjustment of transport errors. **Uncertainties in the radiative transfer inverse modeling underlying the retrieval of XCO<sub>2</sub> yield systematic errors in the XCO<sub>2</sub> data, i.e., errors with spatial correlations.** These errors are a major component of the observation

errors. Their impact on the inversions highly depends on their structure and on the ability, in the inversion systems, to anticipate for such a complex error component (Santaren et al., 2021). We deliberately avoided to account for such error components resulting from numerical models because they can hardly be characterized appropriately by the type of OSSEs conducted here, and because they consist in unknown time-evolving residuals, for which existing studies hardly provide more than qualitative insights, or case-specific values. They tend to diminish along with model and remote sensing progress, in contrast to random errors, which explains the focus of this study on the potential and limitation of the observation systems.

Other types of errors may have been ignored in our inversion configuration while potentially having significant impact. Our reasoning pushed for neglecting the uncertainty in the large- and fine-scale patterns of the initial and boundary conditions. Santaren et al. (2021) showed a low impact of uncertainties in a single scaling factor for the whole initial and boundary conditions of the modeling window and domain at the 6-hour scale and the fine scale patterns are assumed to vanish quickly in time. However uncertainties in the gradients along the boundaries and in synoptic patterns might actually have a large amplitude which persists across the modelling domain and perturbs the identification of atmospheric imprints of the local and regional fluxes. Results have shown that the representation and aggregation errors should be accounted for at the ground observation stations outside the main area of interest, where the spatial transport and inversion resolutions are coarse. These errors might also need to be re-assessed in the high resolution part of the domain but Bréon et al. (2015) used similar transport and control resolutions and they showed that there errors should be low, even at stations at the edge of urban areas. In a more general way, the quantitative results from our experiments, like those from all OSSEs, can suffer from the lack of account for specific sources of errors or for the lack of ability to characterize properly complex ones. However, they support a good understanding of the inversion processes and of the potential of the observation networks.

The use of XCO<sub>2</sub> sampling and error simulations for a day in 2014 while the flux and transport modelling framework corresponds to another day in 2015 raises an inconsistency between the cloud patterns and the meteorological forcing of the atmospheric transport. However, the cloud cover in the selected satellite track is moderate, the gaps due to this cover are spread relatively homogeneously along the track, and a redistribution of these gaps with similar fraction of cloudy scenes should not impact the general results. Similarly, the potential inconsistency between the variations in space of the XCO<sub>2</sub> errors (which are limited, in the range 0.4 to 0.7 ppm) and the atmospheric conditions are assumed to be negligible.

The results, in particular those of the sensitivity tests with and without NEE or nuclear emissions, demonstrate the need for a complex simulation of the CO<sub>2</sub> and <sup>14</sup>CO<sub>2</sub> transport, taking into account the diversity of <sup>14</sup>CO<sub>2</sub> sources and sinks, and more realistic than the common simplification which consists of representing only the dilution of radiocarbon-free FF CO<sub>2</sub> emissions. This and an inversion system at high resolution is more suitable for assessing the real ability to extrapolate information from the <sup>14</sup>CO<sub>2</sub> atmospheric data. However, given its high spatial and temporal resolution, the analytical inversion framework used here can hardly be run over several days, because the size of the matrices to be inverted would become too large. Therefore, inversions have been run for one day only, on July 1 2015 i.e. for very specific atmospheric conditions and biogenic fluxes. In summer the biogenic fluxes are relatively high. Tests over different days, e.g. in winter, could bring a more precise characterization of the complementarity of in situ networks with satellite data, but the primary focus of this study was to investigate the problem of the separation between the biogenic fluxes and FF emissions. By limiting the inversion window

to a single day, we avoid analyzing to which extent the temporal correlations of the uncertainties in the FF CO<sub>2</sub> emission inventories allow for cross-referencing the information of data from different days. This assessment should rely on a strong knowledge on the structures of uncertainties in the FF emissions, which is still incomplete, as illustrated above, even though efforts have been conducted to improve this issue (Wang et al., 2020; Super et al., 2020).

Finally our study tested a surface network roughly corresponding to the extension of a continental network like ICOS for the monitoring of regional FF emission budgets. The deployment of networks dedicated to specific cities with stations around and within the urban areas (Wu et al., 2016) would correspond to a different strategy and could result in different conclusions for the monitoring of city emissions.

## 690 **4.2 Insights from the results**

The results presented here raise contrasting conclusions regarding the potential of the combination between the satellite observation and the surface networks. The satellite observation, as a stand-alone system, can yield estimates of the regional budgets of FF emissions in the morning corresponding to its days of overpass with uncertainties down to 10% (prior 15%, UR 32%) in its FOV. However, it does not provide direct information on emissions during the afternoon or during the night, and it hardly provides information on plants, cities and regions outside its FOV. Furthermore, previous publications (Broquet et al., 2018; Wang et al., 2020; Lespinas et al., 2020; Kuhlmann et al., 2019) have shown that, even with a CO2M constellation of three or more satellites, the number of overpasses producing local images with low cloud cover is limited each year. The data gaps are not random over time and hamper the estimation of annual budgets or their anomalies, as illustrated in the case of the "Great Lockdown" (Chevallier et al., 2020). The need for complementary sources of information to derive daily to annual budgets is thus critical.

The problem of attributing the inferred CO<sub>2</sub> fluxes to specific emission and absorption types appears to be nearly secondary compared to that of the satellite observation precision but our results confirm that there is a significant impact of the uncertainty in the NEE for the estimate of FF emissions. The uncertainty in BF emissions does not appear to have a large impact on the estimate of FF emissions but this is related to the fact that the posterior uncertainty in FF emissions remains larger than the prior uncertainty in BF emissions i.e. to the relatively low level of BF emissions compared to the typical uncertainties in FF emissions at regional to local scales. If the goal is to achieve higher precision estimates of the FF emissions than those obtained with the present configuration, for example with higher precision spaceborne instruments, and if the share of BF emissions increases in the future, the uncertainty in BF emissions would probably become a major problem due to the strong correlation between the spatial distributions of FF and BF emissions. The problem of attribution to NEE fluxes would also increase with this goal of higher precision estimates of the FF emissions in the future.

Surface CO<sub>2</sub>/<sup>14</sup>CO<sub>2</sub> networks can help further decrease the uncertainty in the FF emissions estimates when combined with satellite observations. In North Rhine-Westphalia, the addition of CO<sub>2</sub> and <sup>14</sup>CO<sub>2</sub> stations decreases the posterior uncertainty in daily regional emissions from 8% with the satellite alone to 6.6%. However, relatively dense networks close to highly emitting areas are needed to support such a decrease. The isolated stations far from the urban areas do not provide a direct strong constraint for the estimate of the FF emissions, nor a significant indirect constraint for this estimate by solving for

the attribution problem. Our results suggest that surface CO<sub>2</sub> and/or <sup>14</sup>CO<sub>2</sub> measurements in support of the FF emission monitoring should be targeting FF emission areas directly [and located close to these areas](#) rather than [in the more remote countryside dominated by signals from the NEE](#)~~the surrounding NEE~~. Both hourly CO<sub>2</sub> and daily <sup>14</sup>CO<sub>2</sub> data can provide useful information on the FF emissions, the former catching the signature of these emissions at high frequency and the latter  
720 being much less sensitive to the uncertainty in the NEE.

Overall, the results illustrate a decrease of the potential of each observation subsystem rather than an amplification of these potentials when combining them together into a large observation system with satellite and surface data. This is the natural consequence of the asymptotic convergence of the precision of inversions towards some low value when adding observations. [In our experiments, crossing the spatial extent of the satellite observation, the temporal coverage \(with observations between](#)  
725 [10:00 and 17:00 UTC and a wider temporal representativity\)](#) of the ground-based networks, the temporal resolution ([hourly](#)) of the CO<sub>2</sub> surface network, and the higher sensitivity to FF emissions of the <sup>14</sup>CO<sub>2</sub> network does not lead to the expected synergy with wide spatio-temporal coverage of the FF emissions at high resolution. There is a lack of new extrapolation of information from the combination of observation subsystems. This may be due to the specificities of the attribution and extrapolation problems in our inversion case.

730 Therefore, these results support the deployment of very dense CO<sub>2</sub>/<sup>14</sup>CO<sub>2</sub> surface networks to support the satellite observation, with at least three sites per European administrative region. The large-scale deployment of such dense networks is probably unaffordable in the coming decade, but some regions are now equipped with many stations and in some locations, the complementarity between satellite and surface networks could thus be demonstrated. Frequent (up to daily) samplings of <sup>14</sup>CO<sub>2</sub> would be needed to ensure <sup>14</sup>CO<sub>2</sub> data can bring information on FF emissions more precise than that of hourly CO<sub>2</sub>  
735 measurements.

*Code and data availability.* [The surface fluxes, the emissions, the database for the ground stations and the simulation of the XCO<sub>2</sub> sampling by CO2M in input of our modeling and inversion frameworks are available from the Institutions that are responsible for these products and that are referred to in section 2. The code of the Community Inversion Framework \(CIF\) and its coupling to the CHIMERE model that are used as a basis for our transport modeling framework are available on \[community-inversion.eu\]\(#\).](#)

740 *Author contributions.* 1) writing process: mainly EP, GB, FC with inputs from all co authors, 2) System and experiment design: EP, GB, FC, YW, PC, DS, 3) Implementation: EP, 4) support in development and use of data: AB, IP, FMB, JM 5) Analysis: mainly EP, GB, FC with feedbacks from all co authors

*Competing interests.* The authors declare that they have no conflict of interest.

*Acknowledgements.* This study has been funded by the European Union’s Horizon 2020 research and innovation programme under grant agreements No 776186 (CO<sub>2</sub> Human Emissions project) and 958927 (Prototype system for a Copernicus CO<sub>2</sub> service). This work was granted access to the HPC resources of TGCC under the allocations A0090102201 made by GENCI. We wish to thank Michael Buchwitz and Maximilian Reuter (IUP-UB), as well as Yasjka Meijer and Armin Loescher from from ESA for providing the CO<sub>2</sub>M XCO<sub>2</sub> L2 simulations. The CO<sub>2</sub>M XCO<sub>2</sub> simulations, which were generated in the PMIF study funded by the European Space Agency under Contract No 4000120184. We also thank all the CHE partners and particularly Hugo Denier van der Gon (TNO) for providing the anthropogenic CO<sub>2</sub> inventories, Julia Marshall (MPI-BGC) for providing the biogenic CO<sub>2</sub> fluxes and Tonatiuh Nuñez Ramirez (MPI-BGC) for designing the ground-based network scenario, in the context of WP4 of CHE.

## References

- Agusti-Panareda, A.: The CHE Tier1 Global Nature Run, Tech. rep., CO<sub>2</sub> Human Emissions, H2020 European Project, <https://www.che-project.eu/sites/default/files/2018-07/CHE-D2.2-V1-0.pdf>, 2018.
- 755 Basu, S., Miller, J. B., and Lehman, S.: Separation of biospheric and fossil fuel fluxes of CO<sub>2</sub> by atmospheric inversion of CO<sub>2</sub> and 14CO<sub>2</sub> measurements: Observation System Simulations, *Atmos. Chem. Phys.*, 16, 5665–5683, <https://doi.org/10.5194/acp-16-5665-2016>, number: 9 Reporter: *Atmos. Chem. Phys.*, 2016.
- Basu, S., Baker, D. F., Chevallier, F., Patra, P. K., Liu, J., and Miller, J. B.: The impact of transport model differences on CO<sub>2</sub> surface flux estimates from OCO-2 retrievals of column average CO<sub>2</sub>, *Atmospheric Chemistry and Physics*, 18, 7189–7215, [https://doi.org/10.5194/acp-](https://doi.org/10.5194/acp-18-7189-2018)  
760 18-7189-2018, 2018.
- Basu, S., Lehman, S. J., Miller, J. B., Andrews, A. E., Sweeney, C., Gurney, K. R., Xu, X., Southon, J., and Tans, P. P.: Estimating US fossil fuel CO<sub>2</sub> emissions from measurements of <sup>14</sup>C in atmospheric CO<sub>2</sub>, *Proceedings of the National Academy of Sciences*, 117, 13300–13307, <https://doi.org/10.1073/pnas.1919032117>, 2020.
- Berchet, A., Sollum, E., Thompson, R. L., Pison, I., Thanwerdas, J., Broquet, G., Chevallier, F., Aalto, T., Berchet, A., Bergamaschi, P.,  
765 Brunner, D., Engelen, R., Fortems-Cheiney, A., Gerbig, C., Groot Zwaafink, C. D., Haussaire, J.-M., Henne, S., Houweling, S., Karstens, U., Kutsch, W. L., Luijkx, I. T., Monteil, G., Palmer, P. I., van Peet, J. C. A., Peters, W., Peylin, P., Potier, E., Rödenbeck, C., Saunois, M., Scholze, M., Tsuruta, A., and Zhao, Y.: The Community Inversion Framework v1.0: a unified system for atmospheric inversion studies, *Geoscientific Model Development*, 14, 5331–5354, <https://doi.org/10.5194/gmd-14-5331-2021>, 2021.
- Bergamaschi, P., Frankenberg, C., Meirink, J. F., Krol, M., Villani, M. G., Houweling, S., Dentener, F., Dlugokencky, E. J., Miller, J. B.,  
770 Gatti, L. V., Engel, A., and Levin, I.: Inverse modeling of global and regional CH<sub>4</sub> emissions using SCIAMACHY satellite retrievals, *Journal of Geophysical Research: Atmospheres*, 114, <https://doi.org/10.1029/2009JD012287>, 2009.
- Bieser, J., Aulinger, A., Matthias, V., Quante, M., and Denier van der Gon, H.: Vertical emission profiles for Europe based on plume rise calculations, *Environmental Pollution*, 159, 2935–2946, <https://doi.org/10.1016/j.envpol.2011.04.030>, nitrogen Deposition, Critical Loads and Biodiversity, 2011.
- 775 Broquet, G., Chevallier, F., Rayner, P., Aulagnier, C., Pison, I., Ramonet, M., Schmidt, M., Vermeulen, A. T., and Ciais, P.: A European summertime CO<sub>2</sub> biogenic flux inversion at mesoscale from continuous in situ mixing ratio measurements, *Journal of Geophysical Research: Atmospheres*, 116, <https://doi.org/10.1029/2011JD016202>, 2011.
- Broquet, G., Bréon, F.-M., Renault, E., Buchwitz, M., Reuter, M., Bovensmann, H., Chevallier, F., Wu, L., and Ciais, P.: The potential of satellite spectro-imagery for monitoring CO<sub>2</sub> emissions from large cities, *Atmos. Meas. Tech.*, 11, 681–708, [https://doi.org/10.5194/amt-](https://doi.org/10.5194/amt-11-681-2018)  
780 11-681-2018, number: 2 Reporter: *Atmos. Meas. Tech.*, 2018.
- Bréon, F. M., Broquet, G., Puygrenier, V., Chevallier, F., Xueref-Remy, I., Ramonet, M., Dieudonné, E., Lopez, M., Schmidt, M., Perrussel, O., and Ciais, P.: An attempt at estimating Paris area CO<sub>2</sub> emissions from atmospheric concentration measurements, *Atmos. Chem. Phys.*, 15, 1707–1724, <https://doi.org/10.5194/acp-15-1707-2015>, number: 4 Reporter: *Atmos. Chem. Phys.*, 2015.
- Byrne, B., Liu, J., Yi, Y., Chatterjee, A., Basu, S., Cheng, R., Doughty, R., Chevallier, F., Bowman, K. W., Parazoo, N. C., Crisp, D., Li, X.,  
785 Xiao, J., Sitch, S., Guenet, B., Deng, F., Johnson, M. S., Philip, S., McGuire, P. C., and Miller, C. E.: Multi-year observations reveal a larger than expected autumn respiration signal across northeast Eurasia, *Biogeosciences Discussions*, 2022, 1–28, <https://doi.org/10.5194/bg-2022-40>, 2022.



- Cany, C., Mansilla, C., Mathonnière, G., and da Costa, P.: Nuclear power supply: Going against the misconceptions. Evidence of nuclear flexibility from the French experience, *Energy*, 151, 289–296, <https://doi.org/10.1016/j.energy.2018.03.064>, 2018.
- 790 Chevallier, F., Zheng, B., Broquet, G., Ciais, P., Liu, Z., Davis, S. J., Deng, Z., Wang, Y., Bréon, F.-M., and O’Dell, C. W.: Local Anomalies in the Column-Averaged Dry Air Mole Fractions of Carbon Dioxide Across the Globe During the First Months of the Coronavirus Recession, *Geophysical Research Letters*, 47, e2020GL090244, <https://doi.org/10.1029/2020GL090244>, 2020.
- Ciais, P., Crisp, D., Denier van der Gon, H. A. C., Enge-len, R., Heimann, M., Janssens-Maenhout, G., and Rayner, P., a. S. M.: Towards a European Operational Observing System to Monitor Fossil CO<sub>2</sub> emissions, Tech. rep., European Commission Directorate-General for Internal Market, Industry, Entrepreneurship and SMEs Directorate I – Space Policy, Copernicus and Defence, Brussels, Belgium, <https://doi.org/10.2788/52148>, 2015.
- 795 Ciais, P., Wang, Y., Andrew, R., Bréon, F. M., Chevallier, F., Broquet, G., Nabuurs, G. J., Peters, G., McGrath, M., Meng, W., Zheng, B., and Tao, S.: Biofuel burning and human respiration bias on satellite estimates of fossil fuel CO<sub>2</sub> emissions, *Environmental Research Letters*, 15, 074036, <https://doi.org/10.1088/1748-9326/ab7835>, 2020.
- 800 Crowell, S., Baker, D., Schuh, A., Basu, S., Jacobson, A. R., Chevallier, F., Liu, J., Deng, F., Feng, L., McKain, K., Chatterjee, A., Miller, J. B., Stephens, B. B., Eldering, A., Crisp, D., Schimel, D., Nassar, R., O’Dell, C. W., Oda, T., Sweeney, C., Palmer, P. I., and Jones, D. B. A.: The 2015–2016 carbon cycle as seen from OCO-2 and the global in situ network, *Atmospheric Chemistry and Physics*, 19, 9797–9831, <https://doi.org/10.5194/acp-19-9797-2019>, 2019.
- Degens, E. T.: Biogeochemistry of Stable Carbon Isotopes, pp. 304–329, Springer Berlin Heidelberg, Berlin, Heidelberg, [https://doi.org/10.1007/978-3-642-87734-6\\_14](https://doi.org/10.1007/978-3-642-87734-6_14), 1969.
- 805 Denier van der Gon, H. A. C., Kuenen, J. J. P., Janssens-Maenhout, G., Döring, U., Jonkers, S., and Visschedijk, A.: TNO\_CAMS high resolution European emission inventory 2000-2014 for anthropogenic CO<sub>2</sub> and future years following two different pathways, *Earth System Science Data Discussions*, pp. 1–30, <https://doi.org/10.5194/essd-2017-124>, publisher: Copernicus GmbH, 2017.
- ESA: ESA Annual Report 2015, Tech. rep., ESA, 2015.
- 810 Farquhar, G. D., Ehleringer, J. R., and Hubick, K. T.: Carbon Isotope Discrimination and Photosynthesis, *Annual Review of Plant Physiology and Plant Molecular Biology*, 40, 503–537, <https://doi.org/10.1146/annurev.pp.40.060189.002443>, 1989.
- Fortems-Cheiney, A., Pison, I., Broquet, G., Dufour, G., Berchet, A., Potier, E., Coman, A., Siour, G., and Costantino, L.: Variational regional inverse modeling of reactive species emissions with PYVAR-CHIMERE-v2019, *Geoscientific Model Development*, 14, 2939–2957, <https://doi.org/10.5194/gmd-14-2939-2021>, 2021.
- 815 Graven, H. and Gruber, N.: Continental-scale enrichment of atmospheric <sup>14</sup>CO<sub>2</sub> from the nuclear power industry: Potential impact on the estimation of fossil fuel-derived CO<sub>2</sub>, *Atmospheric Chemistry and Physics Discussions*, 11, 14 583–14 605, <https://doi.org/10.5194/acpd-11-14583-2011>, reporter: Atmospheric Chemistry and Physics Discussions, 2011.
- Graven, H., Allison, C. E., Etheridge, D. M., Hammer, S., Keeling, R. F., Levin, I., Meijer, H. A. J., Rubino, M., Tans, P. P., Trudinger, C. M., Vaughn, B. H., and White, J. W. C.: Compiled records of carbon isotopes in atmospheric CO<sub>2</sub>; for historical simulations in CMIP6, *Geoscientific Model Development*, 10, 4405–4417, <https://doi.org/10.5194/gmd-10-4405-2017>, number: 12 Reporter: Geoscientific Model Development, 2017.
- 820 Graven, H., Fischer, M. L., Lueker, T., Jeong, S., Guilderson, T. P., Keeling, R. F., Bambha, R., Brophy, K., Callahan, W., Cui, X., Frankenberg, C., Gurney, K. R., LaFranchi, B. W., Lehman, S. J., Michelsen, H., Miller, J. B., Newman, S., Paplawsky, W., Parazoo, N. C., Sloop, C., and Walker, S. J.: Assessing fossil fuel CO<sub>2</sub> emissions in California using atmospheric observations and models, *Environmental Research Letters*, 13, 065007, <https://doi.org/10.1088/1748-9326/aabd43>, 2018.
- 825

- Guimberteau, M., Zhu, D., Maignan, F., Huang, Y., Yue, C., Dantec-Nédélec, S., Ottlé, C., Jornet-Puig, A., Bastos, A., Laurent, P., Goll, D., Bowring, S., Chang, J., Guenet, B., Tifafi, M., Peng, S., Krinner, G., Ducharne, A., Wang, F., Wang, T., Wang, X., Wang, Y., Yin, Z., Lauerwald, R., Joetzjer, E., Qiu, C., Kim, H., and Ciais, P.: ORCHIDEE-MICT (v8.4.1), a land surface model for the high latitudes: model description and validation, *Geoscientific Model Development*, 11, 121–163, <https://doi.org/10.5194/gmd-11-121-2018>, publisher: Copernicus GmbH, 2018.
- 830 Hammer, S. and Levin, I.: Monthly mean atmospheric D14CO<sub>2</sub> at Jungfraujoch and Schauinsland from 1986 to 2016, <https://doi.org/10.11588/data/10100>, 2017.
- IPCC: 2019 Refinement to the 2006 IPCC Guidelines for National Greenhouse Gas Inventories, Tech. rep., Calvo Buendia, E., Tanabe, K., Kranjc, A., Baasansuren, J., Fukuda, M., Ngarize, S., Osako, A., Pyrozhenko, Y., Shermanau, P. and Federici, S. (eds), 2019.
- 835 Jung, M., Henkel, K., Herold, M., and Churkina, G.: Exploiting synergies of global land cover products for carbon cycle modeling, *Remote Sensing of Environment*, 101, 534–553, <https://doi.org/10.1016/j.rse.2006.01.020>, 2006.
- Kaminski, T., Rayner, P. J., Heimann, M., and Enting, I. G.: On aggregation errors in atmospheric transport inversions, *Journal of Geophysical Research: Atmospheres*, 106, 4703–4715, <https://doi.org/10.1029/2000JD900581>, \_eprint: <https://agupubs.onlinelibrary.wiley.com/doi/pdf/10.1029/2000JD900581>, 2001.
- 840 Kuhlmann, G., Broquet, G., Marshall, J., Clément, V., Löscher, A., Meijer, Y., and Brunner, D.: Detectability of CO<sub>2</sub> emission plumes of cities and power plants with the Copernicus Anthropogenic CO<sub>2</sub> Monitoring (CO2M) mission, *Atmospheric Measurement Techniques*, 12, 6695–6719, <https://doi.org/10.5194/amt-12-6695-2019>, publisher: Copernicus GmbH, 2019.
- Kuhlmann, G., Brunner, D., Broquet, G., and Meijer, Y.: Quantifying CO<sub>2</sub> emissions of a city with the Copernicus Anthropogenic CO<sub>2</sub> Monitoring satellite mission, *Atmospheric Measurement Techniques*, 13, 6733–6754, <https://doi.org/10.5194/amt-13-6733-2020>, 2020.
- 845 Lee, H., Dlugokencky, E. J., Turnbull, J. C., Lee, S., Lehman, S. J., Miller, J. B., Pétron, G., Lim, J.-S., Lee, G.-W., Lee, S.-S., and Park, Y.-S.: Observations of atmospheric <sup>14</sup>CO<sub>2</sub> at Anmyeondo GAW station, South Korea: implications for fossil fuel CO<sub>2</sub> and emission ratios, *Atmospheric Chemistry and Physics*, 20, 12 033–12 045, <https://doi.org/10.5194/acp-20-12033-2020>, 2020.
- Lehman, S. J., Miller, J. B., Wolak, C., Southon, J., Tans, P. P., Montzka, S. A., Sweeney, C., Andrews, A., LaFranchi, B., Guilderson, T. P., and et al.: Allocation of Terrestrial Carbon Sources Using 14CO<sub>2</sub>: Methods, Measurement, and Modeling, *Radiocarbon*, 55, 1484–1495, <https://doi.org/10.1017/S0033822200048414>, 2013.
- 850 Lespinas, F., Wang, Y., Broquet, G., Bréon, F.-M., Buchwitz, M., Reuter, M., Meijer, Y., Loescher, A., Janssens-Maenhout, G., Zheng, B., and Ciais, P.: The potential of a constellation of low earth orbit satellite imagers to monitor worldwide fossil fuel CO<sub>2</sub> emissions from large cities and point sources, *Carbon Balance and Management*, 15, 18, <https://doi.org/10.1186/s13021-020-00153-4>, 2020.
- Levin, I., Kromer, B., Schmidt, M., and Sartorius, H.: A novel approach for independent budgeting of fossil fuel CO<sub>2</sub> over Europe by 14CO<sub>2</sub> observations, *Geophysical Research Letters*, 30, <https://doi.org/10.1029/2003GL018477>, number: 23 Reporter: *Geophysical Research Letters*, 2003.
- 855 Levin, I., Karstens, U., Eritt, M., Maier, F., Arnold, S., Rzesanke, D., Hammer, S., Ramonet, M., Vítková, G., Conil, S., Heliasz, M., Kubistin, D., and Lindauer, M.: A dedicated flask sampling strategy developed for Integrated Carbon Observation System (ICOS) stations based on CO<sub>2</sub> and CO measurements and Stochastic Time-Inverted Lagrangian Transport (STILT) footprint modelling, *Atmospheric Chemistry and Physics*, 20, 11 161–11 180, <https://doi.org/10.5194/acp-20-11161-2020>, 2020.
- 860 Levin, I., Hammer, S., Kromer, B., Preunkert, S., Weller, R., and Worthy, D. E.: RADIOCARBON IN GLOBAL TROPOSPHERIC CARBON DIOXIDE, *Radiocarbon*, p. 1–11, <https://doi.org/10.1017/RDC.2021.102>, 2021.

- Locatelli, R., Bousquet, P., Saunois, M., Chevallier, F., and Cressot, C.: Sensitivity of the recent methane budget to LMDz sub-grid-scale physical parameterizations, *Atmospheric Chemistry and Physics*, 15, 9765–9780, <https://doi.org/10.5194/acp-15-9765-2015>, 2015.
- 865 López, R., Guillén, J., Fiore, G., M'Barek, R., Tamosiunas, S., Camia, A., Banja, M., Cazzaniga, N. E., Gurría, P., García Condado, S., Jonsson, R., and Ronzon, T.: Biomass flows in the European Union: the Sankey biomass diagram – towards a cross set integration of biomass, Publications Office of the European Union, <https://data.europa.eu/doi/10.2760/352412>, 2017.
- Mahadevan, P., Wofsy, S. C., Matross, D. M., Xiao, X., Dunn, A. L., Lin, J. C., Gerbig, C., Munger, J. W., Chow, V. Y., and Gottlieb, E. W.: A satellite-based biosphere parameterization for net ecosystem CO<sub>2</sub> exchange: Vegetation Photosynthesis and Respiration Model (VPRM), *Global Biogeochemical Cycles*, 22, <https://doi.org/10.1029/2006GB002735>, number: 2 Reporter: *Global Biogeochemical Cycles*, 2008.
- 870 Marshall, J., Nuñez Ramirez, T., and partners, W. C.: Attribution Problem Configurations, Tech. rep., CO<sub>2</sub> Human Emissions, H2020 European Project, <https://www.che-project.eu/sites/default/files/2020-01/CHE-D4-3-V4-1.pdf>, 2019.
- Menut, L., Bessagnet, B., Khvorostyanov, D., Beekmann, M., Blond, N., Colette, A., Coll, I., Curci, G., Foret, G., Hodzic, A., Mailler, S., Meleux, F., Monge, J.-L., Pison, I., Siour, G., Turquety, S., Valari, M., Vautard, R., and Vivanco, M. G.: CHIMERE 2013: a model for regional atmospheric composition modelling, *Geoscientific Model Development*, 6, 981–1028, <https://doi.org/10.5194/gmd-6-981-2013>, 2013.
- 875 Miller, J. B., Lehman, S. J., Montzka, S. A., Sweeney, C., Miller, B. R., Karion, A., Wolak, C., Dlugokencky, E. J., Southon, J., Turnbull, J. C., and Tans, P. P.: Linking emissions of fossil fuel CO<sub>2</sub> and other anthropogenic trace gases using atmospheric <sup>14</sup>CO<sub>2</sub>, *Journal of Geophysical Research: Atmospheres*, 117, <https://doi.org/10.1029/2011JD017048>, number: D8 Reporter: *Journal of Geophysical Research: Atmospheres*, 2012.
- 880 Monteil, G., Broquet, G., Scholze, M., Lang, M., Karstens, U., Gerbig, C., Koch, F.-T., Smith, N. E., Thompson, R. L., Luijkx, I. T., White, E., Meesters, A., Ciais, P., Ganesan, A. L., Manning, A., Mischurow, M., Peters, W., Peylin, P., Tarniewicz, J., Rigby, M., Rödenbeck, C., Vermeulen, A., and Walton, E. M.: The regional European atmospheric transport inversion comparison, EUROCOM: first results on European-wide terrestrial carbon fluxes for the period 2006–2015, *Atmospheric Chemistry and Physics*, 20, 12 063–12 091, <https://doi.org/10.5194/acp-20-12063-2020>, 2020.
- 885 Munassar, S., Rödenbeck, C., Koch, F.-T., Totsche, K. U., Gałkowski, M., Walther, S., and Gerbig, C.: Net ecosystem exchange (NEE) estimates 2006–2019 over Europe from a pre-operational ensemble-inversion system, *Atmospheric Chemistry and Physics*, 22, 7875–7892, <https://doi.org/10.5194/acp-22-7875-2022>, 2022.
- Naipal, V., Ciais, P., Wang, Y., Lauerwald, R., Guenet, B., and Van Oost, K.: Global soil organic carbon removal by water erosion under climate change and land use change during AD 1850–2005, *Biogeosciences*, 15, 4459–4480, <https://doi.org/10.5194/bg-15-4459-2018>, 2018.
- 890 Palmer, P. I., Suntharalingam, P., Jones, D. B. A., Jacob, D. J., Streets, D. G., Fu, Q., Vay, S. A., and Sachse, G. W.: Using CO<sub>2</sub>:CO correlations to improve inverse analyses of carbon fluxes, *Journal of Geophysical Research: Atmospheres*, 111, <https://doi.org/10.1029/2005JD006697>, 2006.
- 895 Peiro, H., Crowell, S., Schuh, A., Baker, D. F., O'Dell, C., Jacobson, A. R., Chevallier, F., Liu, J., Eldering, A., Crisp, D., Deng, F., Weir, B., Basu, S., Johnson, M. S., Philip, S., and Baker, I.: Four years of global carbon cycle observed from the Orbiting Carbon Observatory 2 (OCO-2) version 9 and in situ data and comparison to OCO-2 version 7, *Atmospheric Chemistry and Physics*, 22, 1097–1130, <https://doi.org/10.5194/acp-22-1097-2022>, 2022.

- Pillai, D., Buchwitz, M., Gerbig, C., Koch, T., Reuter, M., Bovensmann, H., Marshall, J., and Burrows, J. P.: Tracking city CO<sub>2</sub> emissions from space using a high-resolution inverse modelling approach: a case study for Berlin, Germany, *Atmospheric Chemistry and Physics*, 16, 9591–9610, <https://doi.org/10.5194/acp-16-9591-2016>, 2016.
- Pinty, B., Janssens-Maenhout, G., Dowell, M., Zunker, H., Brunhes, T., Ciais, P., Dee, D., Denier van der Gon, H. A. C., Dolman, H., Drinkwater, M., Engelen, R., Heimann, M., Holmlund, K., Husband, R., Kentarchos, A., Meyer, A., Palmer, P., and Scholze, M.: An operational anthropogenic CO<sub>2</sub> emissions monitoring and verification support capacity. Baseline requirements, model components and functional architecture, Tech. rep., European Commission Joint Research Centre, Ispra, Italy, <https://doi.org/10.2760/08644>, 2017.
- Portmann, F. T., Siebert, S., and Döll, P.: MIRCA2000—Global monthly irrigated and rainfed crop areas around the year 2000: A new high-resolution data set for agricultural and hydrological modeling, *Global Biogeochemical Cycles*, 24, <https://doi.org/10.1029/2008GB003435>, 2010.
- Reuter, M., Buchwitz, M., Schneising, O., Krautwurst, S., O’Dell, C. W., Richter, A., Bovensmann, H., and Burrows, J. P.: Towards monitoring localized CO<sub>2</sub> emissions from space: co-located regional CO<sub>2</sub> and NO<sub>2</sub> enhancements observed by the OCO-2 and SSP satellites, *Atmospheric Chemistry and Physics*, 19, 9371–9383, <https://doi.org/10.5194/acp-19-9371-2019>, 2019.
- Sadiq, M., Palmer, P. I., Lunt, M. F., Feng, L., Super, I., Dellaert, S. N. C., and Denier van der Gon, H. A. C.: Understanding the influence of combustion on atmospheric CO<sub>2</sub> over Europe by using satellite observations of CO<sub>2</sub> and reactive trace gases, *Atmospheric Chemistry and Physics Discussions*, 2021, 1–34, <https://doi.org/10.5194/acp-2021-816>, 2021.
- Santaren, D., Broquet, G., Bréon, F.-M., Chevallier, F., Siméoni, D., Zheng, B., and Ciais, P.: A local- to national-scale inverse modeling system to assess the potential of spaceborne CO<sub>2</sub> measurements for the monitoring of anthropogenic emissions, *Atmospheric Measurement Techniques*, 14, 403–433, <https://doi.org/10.5194/amt-14-403-2021>, 2021.
- Schuh, A. E., Jacobson, A. R., Basu, S., Weir, B., Baker, D., Bowman, K., Chevallier, F., Crowell, S., Davis, K. J., Deng, F., Denning, S., Feng, L., Jones, D., Liu, J., and Palmer, P. I.: Quantifying the Impact of Atmospheric Transport Uncertainty on CO<sub>2</sub> Surface Flux Estimates, *Global Biogeochemical Cycles*, 33, 484–500, <https://doi.org/10.1029/2018GB006086>, 2019.
- Schwandner, F. M., Gunson, M. R., Miller, C. E., Carn, S. A., Eldering, A., Krings, T., Verhulst, K. R., Schimel, D. S., Nguyen, H. M., Crisp, D., O’Dell, C. W., Osterman, G. B., Iraci, L. T., and Podolske, J. R.: Spaceborne detection of localized carbon dioxide sources, *Science*, 358, eaam5782, <https://doi.org/10.1126/science.aam5782>, 2017.
- Staufner, J., Broquet, G., Bréon, F.-M., Puygrenier, V., Chevallier, F., Xueref-Rémy, I., Dieudonné, E., Lopez, M., Schmidt, M., Ramonet, M., Perrussel, O., Lac, C., Wu, L., and Ciais, P.: The first 1-year-long estimate of the Paris region fossil fuel CO<sub>2</sub> emissions based on atmospheric inversion, *Atmos. Chem. Phys.*, 16, 14 703–14 726, <https://doi.org/10.5194/acp-16-14703-2016>, number: 22 Reporter: *Atmos. Chem. Phys.*, 2016.
- Stuiver, M. and Polach, H. A.: Discussion Reporting of 14C Data, *Radiocarbon*, 19, 355–363, <https://doi.org/10.1017/S0033822200003672>, number: 3 Reporter: *Radiocarbon*, 1977.
- Super, I., Dellaert, S. N. C., Visschedijk, A. J. H., and Denier van der Gon, H. A. C.: Uncertainty analysis of a European high-resolution emission inventory of CO<sub>2</sub> and CO to support inverse modelling and network design, *Atmospheric Chemistry and Physics*, 20, 1795–1816, <https://doi.org/10.5194/acp-20-1795-2020>, publisher: Copernicus GmbH, 2020.
- Tarantola, A.: *Inverse Problem Theory and Methods for Model Parameter Estimation*, Society for Industrial and Applied Mathematics, <https://doi.org/10.1137/1.9780898717921>, 2005.

- 935 Turnbull, J., Rayner, P., Miller, J., Naegler, T., Ciais, P., and Cozic, A.: On the use of  $^{14}\text{CO}_2$  as a tracer for fossil fuel  
CO<sub>2</sub>: Quantifying uncertainties using an atmospheric transport model, *Journal of Geophysical Research: Atmospheres*, 114,  
<https://doi.org/10.1029/2009JD012308>, 2009.
- Turnbull, J. C., Miller, J. B., Lehman, S. J., Tans, P. P., Sparks, R. J., and Southon, J.: Comparison of  $^{14}\text{CO}_2$ , CO, and SF<sub>6</sub> as tracers  
for recently added fossil fuel CO<sub>2</sub> in the atmosphere and implications for biological CO<sub>2</sub> exchange, *Geophysical Research Letters*, 33,  
940 <https://doi.org/10.1029/2005GL024213>, 2006.
- Wang, Y.: The potential of observations of radiocarbon in atmospheric CO<sub>2</sub> for the atmospheric inversion of fossil fuel CO<sub>2</sub> emission at  
regional scale, Ph.D. thesis, Université Paris Saclay, <https://tel.archives-ouvertes.fr/tel-01529200>, 2016.
- Wang, Y., Broquet, G., Ciais, P., Chevallier, F., Vogel, F., Kadygrov, N., Wu, L., Yin, Y., Wang, R., and Tao, S.: Estimation of observation  
errors for large-scale atmospheric inversion of CO<sub>2</sub> emissions from fossil fuel combustion, *Tellus B: Chemical and Physical Meteorology*,  
945 69, 1325–1329, <https://doi.org/10.1080/16000889.2017.1325723>, number: 1 Reporter: *Tellus B: Chemical and Physical Meteorology*, 2017.
- Wang, Y., Broquet, G., Ciais, P., Chevallier, F., Vogel, F., Wu, L., Yin, Y., Wang, R., and Tao, S.: Potential of European  $^{14}\text{CO}_2$   
observation network to estimate the fossil fuel CO<sub>2</sub> emissions via atmospheric inversions, *Atmos. Chem. Phys.*, 18, 4229–4250,  
<https://doi.org/10.5194/acp-18-4229-2018>, number: 6 Reporter: *Atmos. Chem. Phys.*, 2018.
- Wang, Y., Broquet, G., Bréon, F.-M., Lespinas, F., Buchwitz, M., Reuter, M., Meijer, Y., Loescher, A., Janssens-Maenhout, G., Zheng, B., and  
950 Ciais, P.: PMIF v1.0: assessing the potential of satellite observations to constrain CO<sub>2</sub> emissions from large cities and point sources over  
the globe using synthetic data, *Geoscientific Model Development*, 13, 5813–5831, <https://doi.org/10.5194/gmd-13-5813-2020>, publisher:  
Copernicus GmbH, 2020.
- Wenger, A., Pugsley, K., O'Doherty, S., Rigby, M., Manning, A. J., Lunt, M. F., and White, E. D.: Atmospheric radiocarbon mea-  
surements to quantify CO<sub>2</sub> emissions in the UK from 2014 to 2015, *Atmospheric Chemistry and Physics*, 19, 14057–14070,  
955 <https://doi.org/10.5194/acp-19-14057-2019>, 2019.
- Wu, L., Broquet, G., Ciais, P., Bellassen, V., Vogel, F., Chevallier, F., Xueref-Remy, I., and Wang, Y.: What would dense atmo-  
spheric observation networks bring to the quantification of city CO<sub>2</sub> emissions?, *Atmospheric Chemistry and Physics*, 16, 7743–7771,  
<https://doi.org/10.5194/acp-16-7743-2016>, number: 12 Reporter: *Atmospheric Chemistry and Physics*, 2016.
- Zazzeri, G., Yeomans, E. A., and Graven, H. D.: Global and regional emissions of radiocarbon from nuclear power plants from 1972 to 2016,  
960 *Radiocarbon*, pp. 1–15, <https://doi.org/10.1017/RDC.2018.42>, reporter: *Radiocarbon*, 2018.

## Appendix A

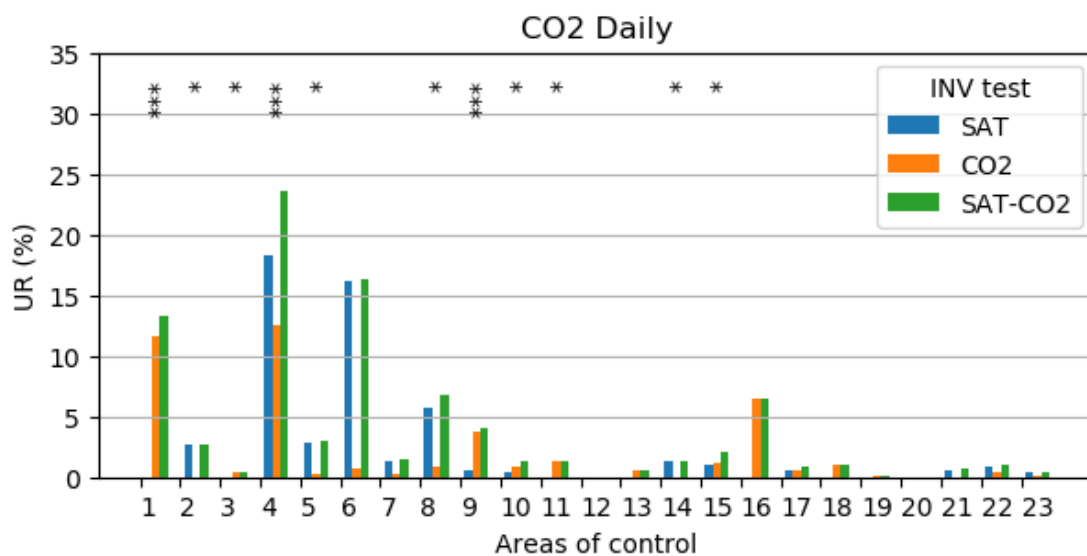


**Figure A1.** Uncertainty reduction in INV-SAT, INV-CO2 and INV-SAT-CO2 inversions for 24-h budgets of FF emissions of each controlled area in the main area of interest. The number of stars indicates the number of stations in each controlled area. The areas are listed in Table 1.

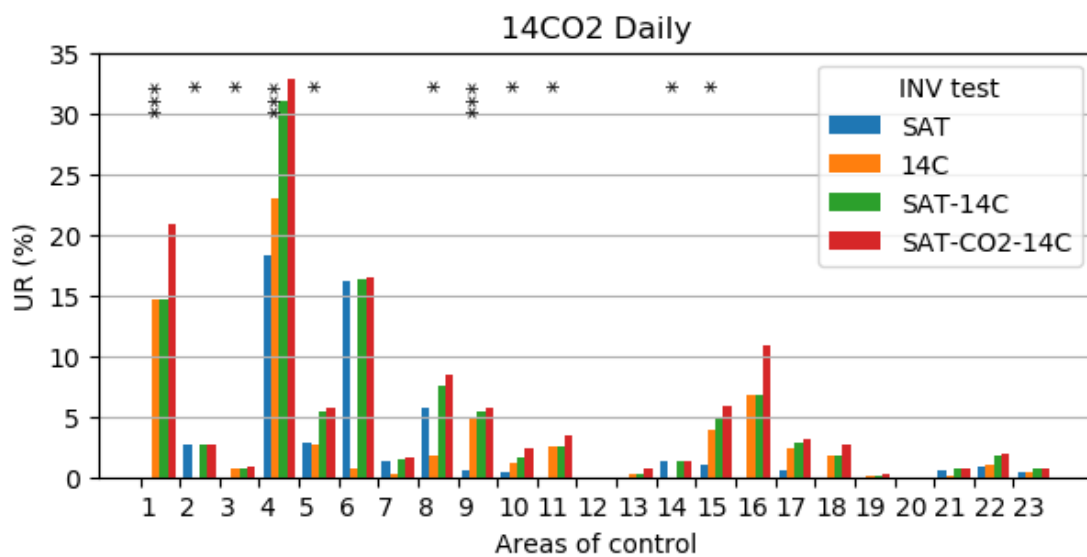


**Figure A2.** Uncertainty reduction in INV-SAT, INV-14C, INV-SAT-14C and INV-SAT-CO2-14C inversions for 24-h budgets of FF emissions of each controlled area in the main area of interest. The number of stars indicate the number of stations in each controlled area. The areas are listed in Table 1.

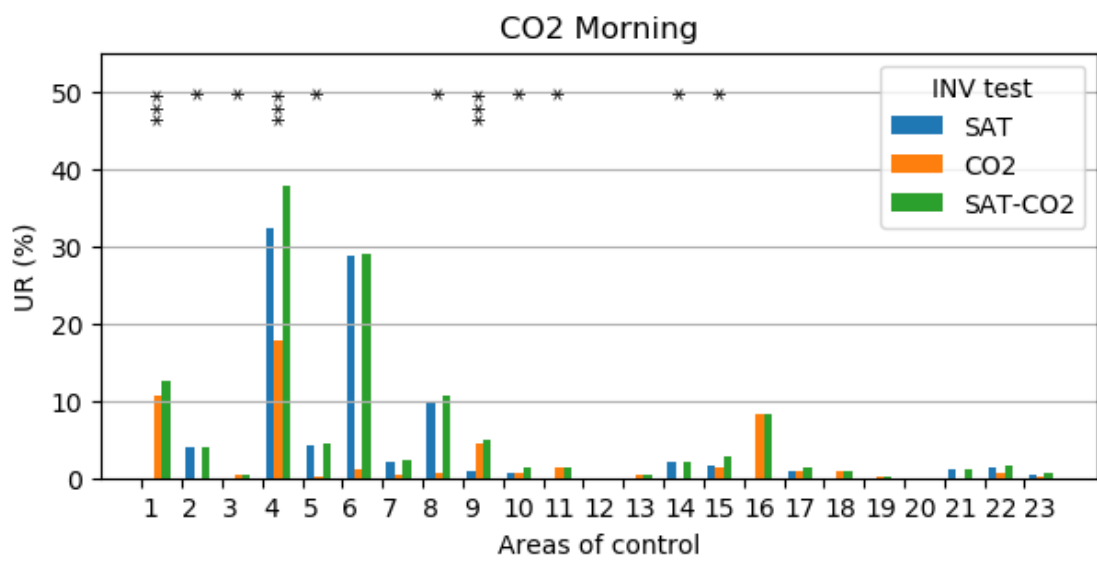


**Figure A3.** Uncertainty reduction in INV-SAT, INV-CO2, INV-SAT-CO2 inversions for morning budgets of FF emissions of each controlled area in the main area of interest. The number of stars indicates the number of stations in each controlled area. The controlled areas are listed in Table 1.



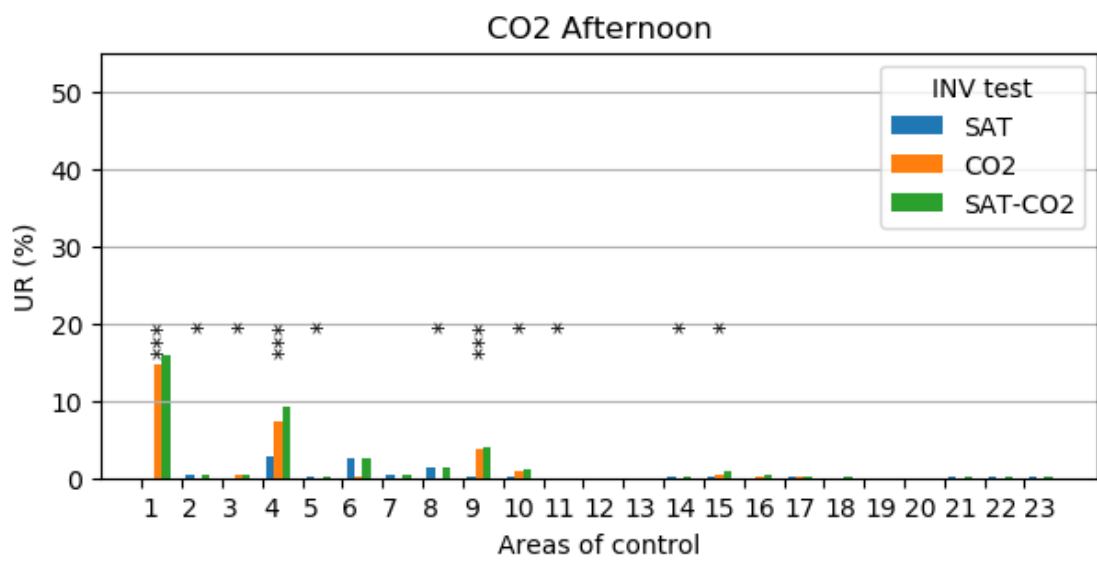


**Figure A4.** Uncertainty reduction in INV-SAT, INV-CO2, INV-SAT-CO2 inversions for afternoon budgets of FF emissions of each controlled area in the main area of interest. The number of stars indicates the number of stations in each controlled area. The names of the controlled areas are listed in Table 1.

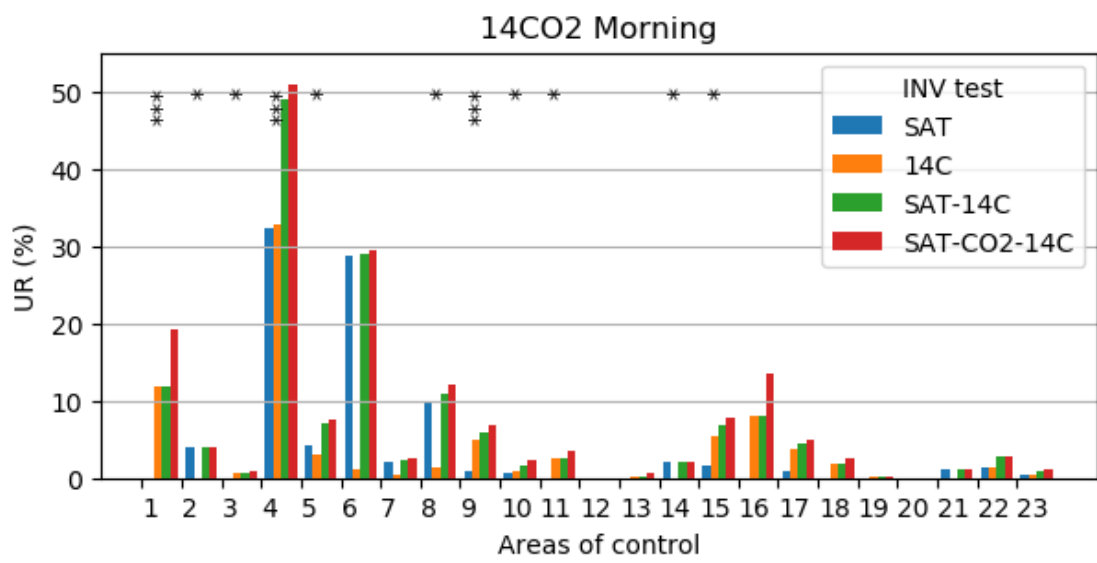


**Figure A5.** Uncertainty reduction in INV-SAT, INV-14C, INV-SAT-14C and INV-SAT-CO2-14C inversions for morning budgets of FF emissions of each controlled area in the main area of interest. The number of stars indicates the number of stations in each controlled area. The names of the controlled areas are listed in Table 1.

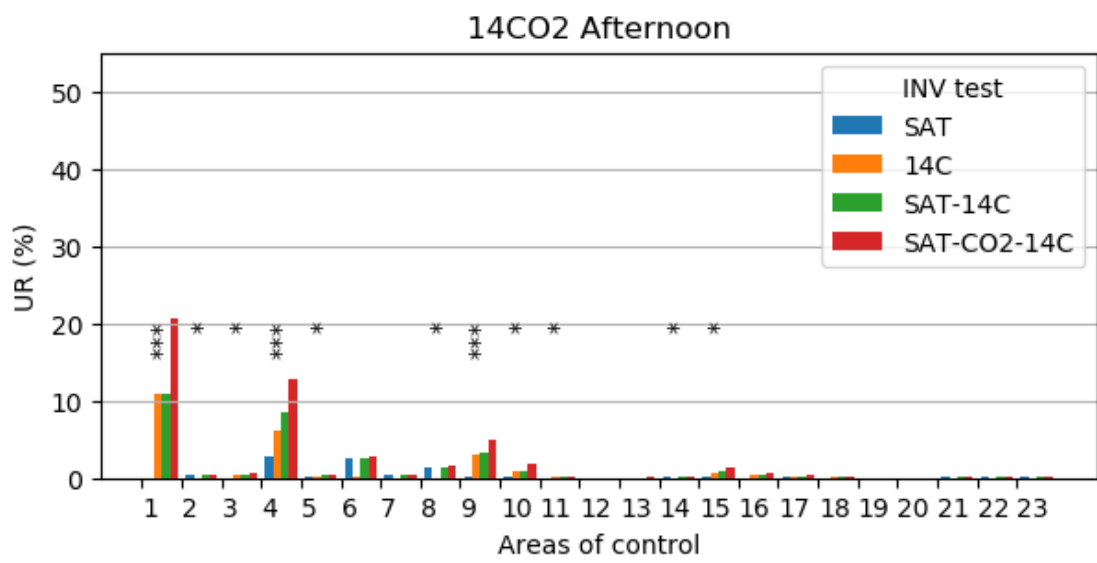
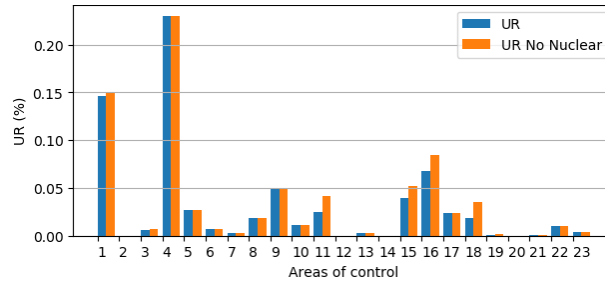
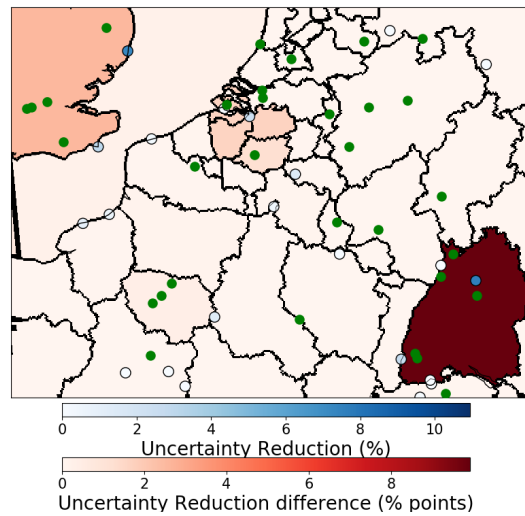


**Figure A6.** Uncertainty reduction in INV-SAT, INV-14C, INV-SAT-14C and INV-SAT-CO2-14C inversions for afternoon budgets of FF emissions of each controlled area in the main area of interest. The number of stars indicates the number of stations in each controlled area. The names of the controlled areas are listed in Table 1.



(a) UR on FF



(b)  $\Delta$ UR on FF budgets and UR on  $F^{14C}$  nuclear power plant budgets

**Figure A7.** (a) Uncertainty reductions, on 24-h FF budgets, with and without nuclear emissions in INV-14C inversion, for each controlled area in the main area of interest. The names of the controlled areas are listed in Table 1. (b) Maps, on the 2-km-resolution area, of the differences between uncertainty reductions with and without nuclear emissions (red palette) in INV-14C inversions and uncertainty reductions on  $F^{14C}$  nuclear power plant budgets (dots, blue palette). Green dots indicate the ground stations.